DEVELOPMENT OF POROUS METAL-SUPPORTED SOLID OXIDE FUEL CELLS

By

Meng Ren, B.E.

A Thesis

Submitted to the school of Graduate Studies

in Partial Fulfillment of the Requirements

for the Degree

Master of Applied Science

McMaster University

MASTER OF APPLIED SCIENCE (2013) McMaster University

MATERIALS SCIENCE AND ENGINEERING Hamilton, Ontario

TITLE: Development of Porous Metal-supported Solid Oxide Fuel Cells

AUTHOR: Meng Ren, B.E. (University of Science & Technology, Beijing)

SUPERVISOR: Dr. Anthony Petric

NUMBER OF PAGES: xvi, 97

Abstract

The introduction of metal supported cells may be a key innovation in the development of solid oxide fuel cell (SOFC) technology. The objective of this study was to develop a process of co-firing the ceramic layers of a solid oxide fuel cell attached to their porous metal support. This is a major departure from the traditional fuel cell architecture where the support layer is a ceramic composite made of YSZ and NiO.

The problems to be eliminated during the fabrication process include the warping, cracking and delamination of the cell during the co-sintering process.

In this study, the porous metal layer was produced by the freeze tape casting process. During co-sintering, it is necessary to match the relative shrinkage between the metal and ceramic layers. Different parameters which can influence the relative shrinkage were explored, including the heating rate, sintering temperature, sintering time, cell thickness, solid loading of the green tapes, applications of wet and dry H_2 in the sintering atmosphere, as well as a change of the electrolyte material. Specifically, GDC was tested as an alternative electrolyte to YSZ.

Since the porous metal substrate is exposed to air during fuel cell operation,

it must be protected from oxidation. Therefore, the pack cementation method was used to apply a layer of aluminum onto the metal substrate. Variables such as temperature and exposure time of the coating materials were investigated in this thesis.

Acknowledgements

I would like to express my gratitude to all those who helped me during the writing of this thesis.

My deepest appreciation and gratitude go first and foremost to my supervisor, Dr. Anthony Petric, for his professional guidance and patient support during the two-year research and study. Thanks for his extraordinary advice, encouragement, trust and confidence he gave me throughout my whole research. He has walked me through all the stages of the writing of this thesis. Without his consistent and illuminating instruction, this thesis could not have reached its present form.

I am extremely grateful to our group member, Dr. Ping Wei, for his good teaching and valuable instructions of the operation details to initiate the research.

Next, my sincere thanks are also due to other members of my research group. Xavier D. Michaud, Simon Joshi, Amin Mali, Yadi Wang and the summer student Cong Peng for providing a supportive and friendly environment in the lab.

In addition, I am grateful for the financial support of NSERC Solid Oxide Fuel Cells Strategic Research Network.

Last my thanks would go to my beloved parents for their loving considerations and great confidence in me all through these years. I also owe my

sincere gratitude to my friends who gave me their help and time in listening to me and helping me work out my problems during the difficult course of the thesis.

Contents

List of Figures

List of Tables

Chapter 1

Introduction

1.1 Motivation and Objectives

Solid oxide fuel cells (SOFCs) have high energy conversion efficiency, better fuel flexibility, less corrosion, less greenhouse gas production and are free from the limitation of the Carnot cycle, with great potential to become the standard for electrical generation in the future. Metal-supported SOFCs which consist of ceramic layers on a stainless steel support are a new concept for fuel cell design. The metal substrate has higher thermal shock resistance and is less sensitive to environmental changes (Brandon et al., 2004). In addition, the lower cost and the strong mechanical properties of the metal substrate are also advantageous.

However, a series of problems emerge when the metal is used as a supporting layer. These challenges include the need for reducing atmosphere during high

temperature sintering, delamination of different layers during the co-sintering process and Cr poisoning during fuel cell operation. Trying to match the relative shrinkage of the metal layer with that of the electrolyte has constituted the main challenges in this thesis. One approach to overcome the problem was to substitute GDC for YSZ as the electrolyte to improve fabrication of the whole cell structure.

As the catalyst, lanthanum strontium manganese oxide (LSM), in the cathode is unstable to the reducing environment at high temperature, the infiltration method was applied after high temperature sintering.

Goward (1998) demonstrated that a pack cementation method can be utilized to increase the oxidation resistance of samples at high temperatures by coating aluminum onto the metal substrate. This approach was followed to provide oxidation resistance for the porous metal support.

This thesis will review the development of the metal-supported SOFC and the pack cementation process. The project concentrates on the co-sintering of all cell layers and the major objectives of the thesis are exploring the influences of different parameters during co-sintering for YSZ SOFC and investigating the alternative GDC material as the electrolyte. In addition, there was a minor objective to optimize the aluminum coating by pack cementation on the metal support.

1.2 Organization of the Thesis

Background and structure of the solid oxide fuel cell are introduced in the second chapter, with particular attention paid to the metal-supported solid oxide fuel cell. Chapter three reviews the fabrication procedures of the cell and the pack cementation process. Chapter four introduces the detailed experimental techniques are reported. In chapter five, the relative shrinkage measurements are displayed and discussed. The results from the co-sintering of the cells are shown and different parameters which can influence the cell are discussed in chapter six. Chapter seven explores the structural characterization of the GDC SOFC and the metal substrate after pack cementation.

Chapter 2

The Solid Oxide Fuel Cell

2.1 Solid Oxide Fuel Cell Overview

The solid oxide fuel cell has high energy conversion efficiency, better fuel flexibility and no need for expensive catalysts. The solid oxide fuel cell has a ceramic solid electrolyte. In addition to the electrolyte, the two electrodes are also solid-state in the SOFC system. As in all electrochemical devices，the electrolyte of the fuel cell system must be permeable to at least one kind of ion among all the species. The electrochemical processes can be explained by the following reactions:

$$\text{Anode:} \quad 2H_2 + 2O^{2-} = 2H_2O + 4e^- \tag{2.1}$$

$$\text{Cathode:} \quad O_2 + 4e^- = 2O^{2-} \tag{2.2}$$

$$\text{Overall:} \quad 2H_2 + O_2 = 2H_2O \tag{2.3}$$

At the anode, H_2 is the reductant which undergoes an oxidization reaction and at the same time, O_2 is the oxidant which goes through a reduction reaction in the cathode. As the electrons flow from anode to cathode, the current can be used for an external electric load, where the anode is negative and the cathode is positive. However, practical problems like the high fabrication cost make the process difficult to commercialize. By lowering the operating temperature from 800℃ towards 500℃, the cost is reduced and the lifetime of the whole cell system is increased because of fewer reactions among the components. However, the increasing electrochemical resistance in the electrolyte and electrocatalytic efficiency of the electrode will reduce the power output. For the higher temperatures up to 1000℃, Shao et al. (2012) reported that the increased electrode reaction kinetics contribute to decreasing ohmic drop, but sintering and reaction between the cell components are also accelerated.

2.2 Interconnect

The electrochemical parts of the SOFC are the porous cermet anode, the dense ceramic electrolyte and the porous oxide cathode. This single cell is used as the power unit that produces about 1V. It can be interconnected to build stacks with

higher voltage (Minh and Takahashi, 1995) as shown in Figure 2.1.

The interconnect separating the anode and the cathode is used as a current collector which has a high chemical stability and conductivity. Stainless steel has proven to be a good candidate for interconnects at intermediate temperature from 500℃ to 800℃ (Fergus, 2005), which is less expensive than other metallic materials and performs well during the process. However, problems still exist as the ferritic stainless steel is easily oxidized by air and the Cr component in the metallic material is easy to volatilize, which will poison the cathode. These issues can be overcome by adding a thin, dense conductive coating on the air side of the metallic interconnect, which contacts with the cathode atmosphere (Minh, 1993, b).

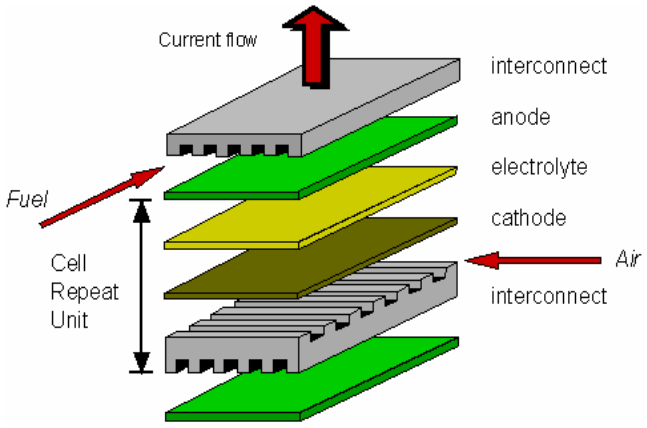

Figure 2.1: Structure of stack (Minh and Takahashi, 1995).

As the interconnect composition is the same as the metal support layer which will be introduced in Section 2.5.2, the details of Cr poisoning will be investigated in that part. In addition, the interconnect is a key part of the system but not the focus of this project, so it will not be discussed further.

2.3 Electrolyte

The electrolyte is essential for conducting the oxygen ions from cathode to anode and separating the different gases on each side. Furthermore, it should also be stable in both oxidizing and reducing environments. Finally, as the electrolyte is the limiting factor in designing the whole cell structure, other components should also be chemically compatible with the electrolyte as the cell will be sintered at high temperature (more than 1000℃) and operated at intermediate temperature (500-800℃).

2.3.1 YSZ Materials

Based on the requirements of electrolyte above, yttria stabilized zirconia (ZrO_2–Y_2O_3), abbreviated as YSZ, is the most suitable. However, it is the

physical properties of the YSZ electrolyte that mainly determine the temperature of operation of the whole cell as the ionic conductivity of YSZ will increase with temperature. Pure ZrO_2 which has a monoclinic crystal structure at room temperature, will change to a tetragonal form when heated above 1170℃, but the monoclinic/tetragonal transformation is reversible, accompanied by expansion during cooling and contraction during heating. This transformation leads to fracture when the material is cooled after sintering. Therefore, a phase with long-term stability is necessary such as the cubic phase, but it is stable only from 2370 to 2680℃ (the melting point of ZrO_2) (Minh and Takahashi, 1995).

When an aliovalent (divalent or trivalent) oxide such as Y_2O_3 (Y^{3+}) is added to pure ZrO_2 (Zr^{4+}), the cubic fluorite structure of ZrO_2 becomes stable from room temperature to its melting point (Scott, 1975). In addition, when the Y^{3+} ions substitute for Zr^{4+} ions, oxygen vacancies are produced which contribute to the higher oxygen-ion conduction as equation (2.4) shows below:

$$Y_2O_3 \rightarrow 2Y'_{Zr} + V_{\ddot{O}} + 3O^{\chi}_{O} \qquad (2.4)$$

The addition of the aliovalent oxides has two functions: to stabilize the cubic fluorite form of ZrO_2, and to enhance the ionic conductivity at the same time (Minh and Takahashi, 1995).

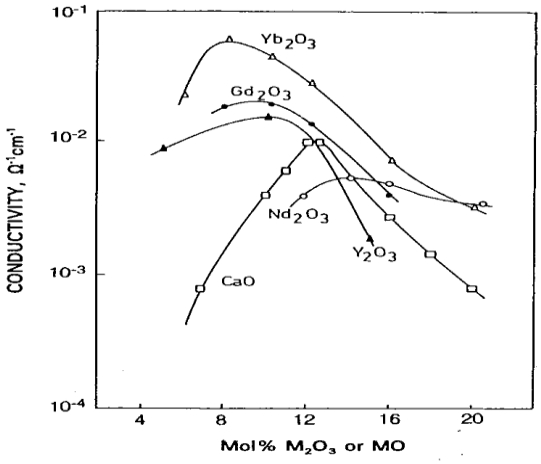

Figure 2.2: Variation of ionic conductivity of stabilized ZrO_2 with dopant concentration at 1080 K (Van de Graaf and Burggraaf, 1984).

The concentration of the dopant plays an important role in the conductivity of stabilized ZrO_2 (Van de Graaf and Burggraaf, 1984). As illustrated in Figure 2.2, the conductivity of any dopant follows a normal distribution. The conductivity increases with concentration at the beginning, and then passes a maximum before decreasing with further addition of dopant. For ZrO_2–Y_2O_3, Takahashi and Suzuki (1967) demonstrated that a maximum conductivity appears between 8 and 10 mol%. Y_2O_3 is added into ZrO_2 to stabilize the cubic fluorite phase and 8 mol% is the minimum quantity of Y_2O_3 observed from Figure 2.2 (Stubican et al., 1978). Therefore, the YSZ with 8 mol% Y_2O_3 is used for the electrolyte, designated as 8YSZ.

2.3.2 GDC Materials

An alternative electrolyte material is cerium oxide. Unlike ZrO_2, pure CeO_2 maintains the cubic fluorite structure from room temperature to the melting point without the addition of dopants. Cerium oxide is usually written as $CeO_{2-\delta}$ (δ is less than 0.3) because of oxygen deficiency. However, the extremely low ionic conductivity of pure CeO_2 can't meet the requirements. Consequently, doping with a trivalent oxide such as Gd_2O_3 forms a solid solution with high ionic conductivity, which is even higher than that of the stabilized ZrO_2 (Minh and Takahashi, 1995).

The conductivity of gadolinia doped ceria (GDC) at 700℃ is approximately equal to that of YSZ at 1000℃, which is the reason that GDC is the main alternative material (Zha et al., 2003). Many advantages are realized by lowering the operating temperature of SOFCs: the lifetime of SOFCs can be extended, the material durability and strength of the product are increased, more suitable candidate materials of the electrodes become available, the degradation of SOFC components is reduced (Brandon et al., 2004) and the sealing problem becomes much easier to solve as well as the cost during processing and sintering is decreased.

Reducing the thickness of the YSZ electrolyte and using the GDC as a substitute are two methods mentioned by Zha et al. (2003) to decrease the operating temperature by lowering the resistance of dense electrolyte membrane. In addition, when GDC is mixed with LSM, the electrode polarization resistance is reduced and the electro catalytic activity of the LSM electrode is increased, thus changing the electrode behavior (Jiang and Wang, 2005).

Although GDC has many advantages, YSZ is superior because it's the material with 100% ionic conductivity while GDC has a fraction of electronic leakage. When YSZ is utilized as the electrolyte, if the external current is interrupted, the ion transport will stop immediately in the fuel cell. Conversely, for the GDC fuel cell, if the same condition occurs (the external current route is interrupted), the electrons will flow through the electrolyte as it's not the 100% ionic. Secondly, YSZ is less costly than GDC. As a result, both YSZ and GDC fuel cells are of value to be investigated in our research because each of the two materials has its own advantages and disadvantages.

2.4 Cathode and Anode

Similar to the electrolyte, the materials of electrodes should be stable in oxidizing or reducing atmosphere. Moreover, there should be no phase transformation in the

cathode and anode, and the materials should be compatible with other components and have high electronic conductivity. Unlike the electrolyte, the cathode and anode structures should be porous, so that the gas can go through. Doped $LaMnO_3$ is usually applied as the cathode material because it meets the requirements of low cost (Minh and Takahashi, 1995). The requirements of electrolyte, cathode and anode are shown in Table 2.1.

Table 2.1: Comparisons among the three basic components of a fuel cell.

	Electrolyte	Cathode	Anode
Stability	•Be stable in reducing and oxidizing atmosphere •No disruptive phase transformation	•Be stable in oxidizing atmosphere •No disruptive phase transformation	•Be stable in reducing atmosphere •No disruptive phase transformation
Conductivity	•Sufficient ionic conductivity •Negligible electronic conductivity	Sufficient electronic conductivity	Sufficient electronic conductivity
Compatibility	Be compatible with other components	Be compatible with other components	Be compatible with other components
Thermal Expansion	To be matched with other components to avoid cracking and delamination	To be matched with other components to avoid cracking and delamination	To be matched with other components to avoid cracking and delamination
Porosity	No connected porosity	Connected porosity	Connected porosity
Catalytic Activity		Sufficient catalytic activity	Sufficient catalytic activity

Different components deposited on the anode have different functions. For

example, when Ni-YSZ is utilized, Ni is the catalyst and also the electrical conductor. YSZ is added to the anode to meet the requirements of the triple phase boundary which will be introduced in Section 3.4 besides the function of separating Ni particles and to match the shrinkage rate with that of the YSZ electrolyte. During fabrication, the anode is applied as a slurry of NiO-YSZ, and then co-sintered with the electrolyte and cathode layers (Atkinson et al., 2004). The Ni-YSZ is reduced from NiO-YSZ. As the density of NiO is 6.72 g/cm^3 while Ni is 8.88 g/cm^3, when NiO is reduced to Ni, the particles will shrink and consequently the porosity will increase.

2.5 Metal-supported SOFCs

Usually a thick layer is needed as part of the cell for structural support. The SOFCs can be classified into anode-supported, cathode-supported or electrolyte-supported SOFCs according to which material is the supporting layer (Shao et al., 2012).

For traditional anode supported cells, a thicker supporting layer leads to a stronger mechanical structure. However, the layer is made from ceramic or cermet which is expensive, brittle and prone to failure upon redox cycling. The use of a

metal support eliminates these problems and is cheaper as well (Figure 2.3).

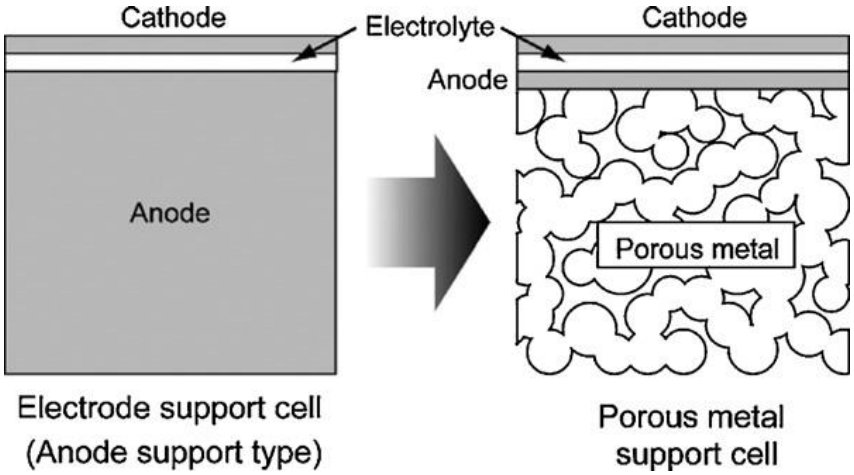

Figure 2.3: Schematic representation of anode-supported cell (ASC) and metal-supported cell (MSC). Only a thin portion of the anode layer, as required for electrochemical function is retained in the MSC design (Tucker, 2010).

2.5.1 Structure of Metal-supported SOFCs

The conventional anode support has low tolerance for thermal shock when undergoing rapid temperature change because of its brittle nature and fractures with rapid temperature cycling. Furthermore, Ni-YSZ supported cells can fail during redox cycling even with slow-heating because of their ceramic structure. When a thick porous stainless steel support is utilized in place of the ceramic or cermet of the traditional fuel cell, the metal has higher thermal shock resistance and is less sensitive to environmental changes (Brandon et al., 2004).

The metal-supported SOFC has the advantage over the conventional

all-ceramic SOFC of low cost and stability. The mechanical strength and gaseous permeability of the metal-supported substrate layer should be adjusted to be compatible with other parts (Brandon et al., 2004). Figure 2.4 shows a cell cross section consisting of metal support, YSZ cathode interlayer, YSZ electrolyte film and YSZ anode interlayer, where all of the other layers are porous except for the dense electrolyte film.

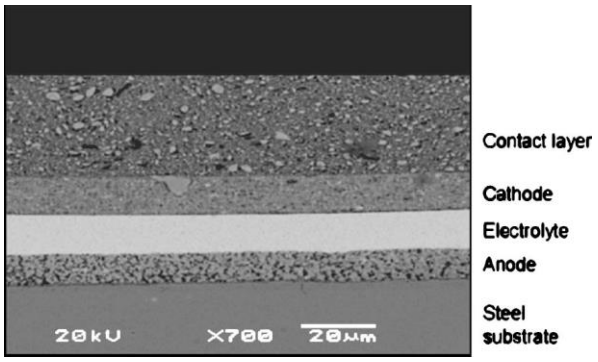

Figure 2.4: Polished cross-section through a metal supported ITSOFC, after testing on moist hydrogen/air at temperatures up to 600℃ (The layer of steel is proved to be porous in the center while impermeable around the edges) (Tucker et al., 2007).

2.5.2 Cr Poisoning Problem

FeCr-based ferritic stainless steels are commonly used for the metal support because of their low cost, high temperature oxidation resistance as well as similar thermal expansion with that of YSZ, which was discussed by Tucker et al. (2007). The Cr content in the ferritic stainless steel is generally between 10.5 wt% and 26

wt%. Al can be added and oxidized to Al_2O_3, serving as a protective layer on the steel surface, which is helpful to resist further oxidization. Table 2.2 shows the percentage of the elements in UNS 430 and UNS 440 stainless steels.

However, porous metal supports have their own challenges of Cr poisoning of the cathode and matching the shrinkage rate of the metal support with that of the electrodes during co-sintering (Christiansen et al., 2006).

Table 2.2: Components of stainless steels used in metal support for SOFC (Bateni et al., 2011).

Element	Weight Percent	
	430 Stainless steel (wt %)	440 Stainless steel (wt %)
Cr	16-18	16-18
Mn	< 1	< 1
Si	< 1	< 1
P	< 0.04	< 0.04
S	< 0.03	< 0.03
C	0.12	0.95-1.2
Mo	-	0.75
Fe	Remainder	Remainder

As mentioned before, Cr is oxidized to Cr_2O_3 when the stainless steel is applied as metal support or interconnect. The presence of Cr content in stainless steel can control oxidation and still conduct electrons. Chromium poisoning occurs because volatile hexavalent chromium will form and migrate to the cathode, causing degradation of cell performance as is illustrated in the equations

below (Ebbinghaus, 1993; Hilpert et al., 1996):

$$2Cr_2O_3 + 3O_2 \Leftrightarrow 4CrO_3\,(g) \quad (2.5)$$

$$2Cr_2O_3 + 3O_2 + 4H_2O \Leftrightarrow 4CrO_2(OH)_2\,(g) \quad (2.6)$$

CrO_3 and $CrO_2(OH)_2$ are examples of two volatile species which are formed by a combination of oxygen and humidity. This explains why there is negligible volatile chromium in the anode. The volatile species are transported from the interconnect to the interface of the electrolyte and cathode and then reduced to Cr_2O_3 in the cathode. The growth of Cr_2O_3 leads to high resistance in the cell stack (Huang and Goodenough, 2009).

As for the interconnect, Trebbels et al. (2009) reported that a protective ceramic coating is needed on the cathode side to isolate Cr from air, which is helpful to maintain electrical conductivity and prevent the formation of chromium (VI). It has been shown that the coating can help alleviate the Cr-poisoning problem (Christiansen et al., 2006). The spinel oxides and perovskite oxides are both common materials for coating because of their significant electronic conductivity in air and ability to retain chromium, but the perovskite oxides have higher cost and more difficulities to be applied as coating (Petric and Ling, 2007).

Chapter 3

Review of Fabrication Methods

The properties of SOFCs are significantly affected by the fabrication process. The freeze tape casting technique was used to prepare the metal support layers which are known as green tapes, on which anode, electrolyte and cathode layers are deposited step by step. Within these functional layers, high porosity is necessary for better gas diffusion throughout the bulk material, except the electrolyte layer. After the organic binder is removed from the green tapes by the burn out procedure, the cell undergoes a high temperature (above 1000℃) co-sintering process, contributing to the strong bonding between the YSZ matrix and the YSZ electrolyte, and the Ni-YSZ anode. Since the LSM cathode cannot survive the high temperature reducing atmosphere, it is infiltrated into the YSZ matrix from

aqueous solution and then calcined and sintered at somewhat lower temperature (800℃).

3.1 Freeze Tape Casting Process

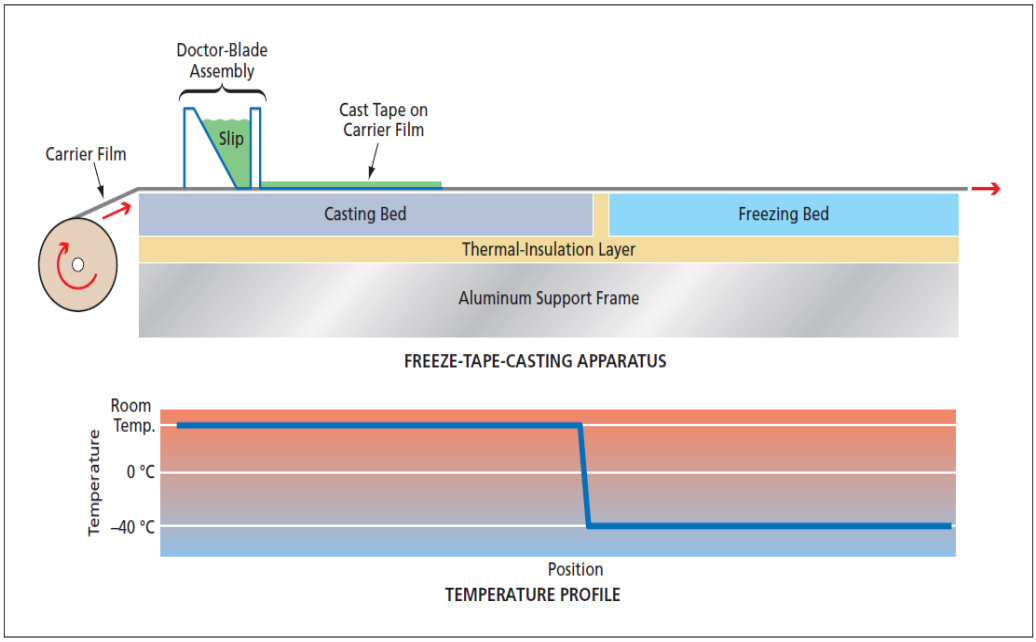

Figure 3.1: In freeze tape casting, a slip is cast into a tape as in traditional tape casting, but then, unlike traditional tape casting, the water and any other solvents in the tape are frozen. The frozen tape is then freeze-dried before sintering. (Temperature profile is indicated for an aqueous system) (Sofie and Dogan, 2001)

As illustrated in Figure 3.1, the freeze tape casting process begins with traditional tape casting of a slurry containing organic binders onto a plateau, controlled by a doctor blade, followed by a freezing step to obtain unidirectional solidification. By applying this method, continuously graded pores and the

long-range alignment of pores are both achievable, which are an aid for gas diffusion.

The tape casting process can be utilized to produce thin ceramic tapes from a slurry. The wide applications of porous ceramics in the fabrication of catalyst-supported structures and filtration membranes demonstrate the importance of traditional tape casting. Corbin and Apte (1999) studied the drawbacks associated with the traditional tape casting technique, in which the pore structures are dependent on the morphology and the packing of fugitive phase materials which are burned out during firing. Sofie and Dogan (2001) showed that the pore structures are influenced by the application of thermal fugitive particle orientation and stability. In addition, the drying process also restricts the tape thickness because of the settling and drying stresses. This technique can be further improved by being combined with freeze casting to achieve better properties.

The freeze tape casting process is useful for tailoring the pore structures in complex-shaped advanced ceramics. Halloran (2006) discussed that the directional solidification of the solvent aligns dendrites bottom to top and the following freeze drying process eliminates the solvent while maintaining the porous structure. Freeze tape casting has distinct advantages over traditional tape casting. Sofie and Dogan (2001) mentioned that the anti-freeze additives such as alcohols in aqueous systems result in a high green density and particle packing after solidification. Moreover, the freeze tape cast pore structures are highly

suitable for porous supports and thick anodes of the solid oxide fuel cell because of the line-of-sight pore channels. Moritz and Richter (2006) also proposed that the tape solidifies quickly, yielding a uniform product. The freeze casting process is useful for the fabrication of thick tapes such as porous substrates for SOFC supports (Moritz and Richter, 2006).

3.2 Screen Printing

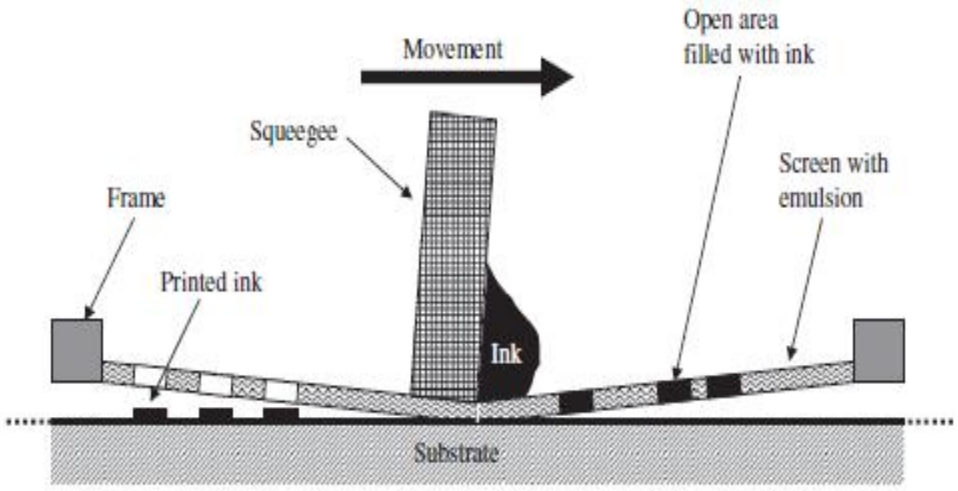

Figure 3.2: Illustration of the screen-printing process (Krebs, 2009).

The freeze tape casting technique is used to produce the thick-films, while screen printing is for adding thin electrode or electrolyte layers. In the screen printing technique, a woven mesh is applied to support an ink-blocking stencil. The open areas of mesh with different shapes which can be designed on the stencil,

allow the transfer of the printable solution as well as the formation of the shaped image on the substrate by traversing with a squeegee. As a result, when the squeegee strokes pass over the screen stencil, the ink is forced into the opening areas of the mesh as illustrated in Figure 3.2.

3.3 Burning out and Co-sintering

When all the cell layers are deposited by tape casting and screen printing, the cell is ready for sintering. First, a step of slow heating is necessary to burn out the binder, followed by a sintering step at high temperature in order to achieve the fully dense layer of electrolyte.

The all-ceramic system can be sintered at high temperature of 1300℃ in air. However, when the metal-support layer is applied, co-sintering in a reducing atmosphere like H_2 must be applied to protect the metal from being oxidized.

3.4 Triple Phase Boundary

The triple phase boundary is the active site where the ionic conductor (electrolyte),

electronic conductor and gas phase all make contact, at which the oxygen reduction reaction and the hydrogen oxidation reaction occur (O' Hayre et al., 2005). An optimized fuel cell should maximize the triple phase boundary area which allows more reactions producing more current flow.

At the triple phase boundary of the anode, O^{2-} ions are supplied to the reaction site through the YSZ ionic conductor and electrons are transported out by the Ni electronic conductor, allowing a neutral reaction available in the pore with molecular hydrogen (Figure 3.3). At the cathode, O^{2-} ions are generated from O_2 gas by the addition of electrons supplied through the LSM electronic conductor and then transported through the YSZ electrolyte to the anode (Figure 3.4). The active area of the triple phase boundary is a one-dimensional line.

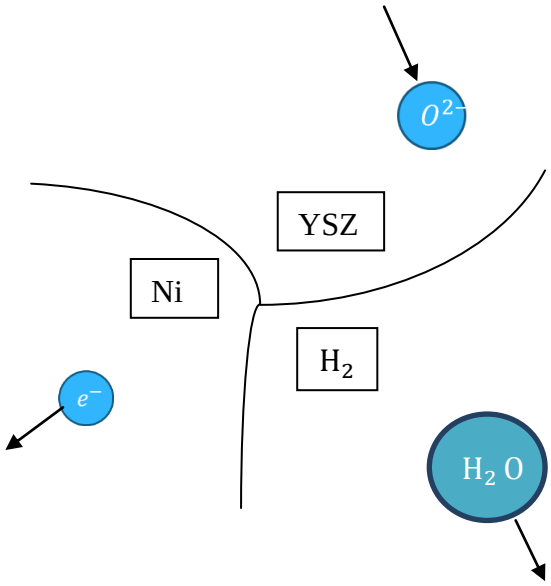

Figure 3.3: Triple phase boundary in anode.

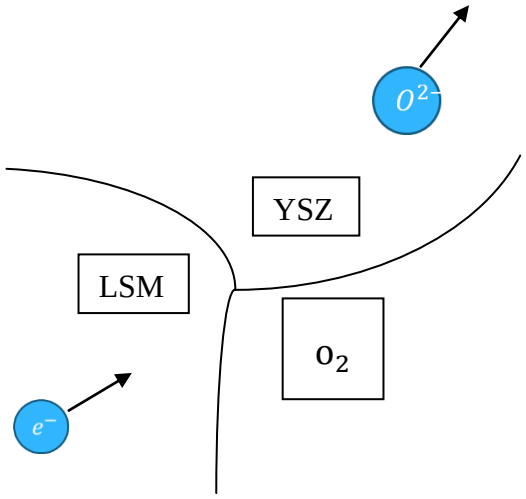

Figure 3.4: Triple phase boundary in cathode.

The porosity provides the volume for the gas phase in the triple phase boundary and is determined by the amount of organic pore former added to the mixture during sample preparation. It is influenced by a few factors, among which shrinkage is the most important one. The shrinkage is inversely proportional to the porosity in some situations; the smaller metal particles may decrease the final porosity and increase the shrinkage rate to match that of the YSZ at the same time. Most importantly, the percentage of the porosity is increased with the content of the binder and the pore former while the shrinkage is reduced (Tucker, 2010).

Finally, higher temperature contributes to lower porosity.

3.5 Pack Cementation

Pack cementation is a relatively new technique to coat aluminum onto the metal substrates. When porous stainless steel is used as the substrate material, the aluminum must permeate all the pores in order to achieve complete coating coverage including the innermost parts of the porous structure. Pack cementation can be applied for coating both porous and non-porous sample surfaces. In the case of the metal support, most of the pores are open, which means that the pore channels are connected.

As mentioned before, a porous structure of the substrate is necessary to form a passage for the gas flow and reaction. However, the pack cementation process will block the pores when applied in excess as more oxidization products are formed in the pore structures than in the flat and dense substrates. The pore size of 10-50 microns is desirable, as smaller pores are not continuous and larger ones can not support the screen printed ceramic layer.

At high temperature (above 800℃), ferritic stainless steel has insufficient oxidation resistance, so the addition of the coatings helps to extend the lifetime of

the SOFCs as well as to prevent the chromium poisoning. However, there are some disadvantages of the Al infiltration. As the function of the cell is to provide a sustained electric current, the components of the cell must be conductive, but Al_2O_3 is an insulator. Therefore, the processing of the cell must include a step where the electrical contact between cells can be reestablished.

There are a few methods which can be used to form an aluminum coating on the ferritic stainless steel, such as ion implantation, hot dipping, electrolysis in fused salt as well as pack cementation. Here the pack cementation is used because of its simple operation and popular use for samples of different sizes and shapes, and even porous substrates (Sivakumar and Rao, 1982). Furthermore, Goward (1998) found that it is useful in increasing the oxidation resistance of samples at high temperatures by adding Al coating.

During the pack cementation process, a metal powder in the mixture is utilized as the source of material for the coating, alumina as a permeable separator and a catalytic agent as a source of metal halides. NH_4Cl decomposes during the heating process as follows:

$$NH_4Cl\ (g) = NH_3(g) + HCl(g) \quad (3.1)$$

$$2NH_3\ (g) = N_2\ (g) + 3H_2\ (g) \quad (3.2)$$

A series of aluminum-halide compounds are generated from the aluminum powder and the halide compounds form according to the following reactions:

$$2Al\ (l) + 2HCl\ (g) = 2AlCl\ (g) + H_2\ (g) \quad (3.3)$$

$$Al\ (l) + 2HCl\ (g) = AlCl_2\ (g) + H_2\ (g) \quad (3.4)$$

$$2Al\ (l) + 6HCl\ (g) = 2AlCl_3\ (g) + 3H_2\ (g) \quad (3.5)$$

The aluminum halide compounds are vapor species, thus allowing diffusion to the surface of the sample. The reactions can then occur at the interface where AlCl and $AlCl_2$ are both oxidized to $AlCl_3$ according to the following equations (Koo, 2004):

$$3AlCl\ (g) \leftrightarrow AlCl_3\ (g) + 2Al(s) \quad (3.6)$$

$$3AlCl_2\ (g) \leftrightarrow 2AlCl_3\ (g) + Al(s) \quad (3.7)$$

At the same time, there is also a reaction on the substrate as follows:

$$2AlCl_3\ (g) + 6Fe\ (s) \leftrightarrow 2Fe_3Al\ (s) + 3Cl_2\ (g) \quad (3.8)$$

Some factors will influence the coating and deposition process such as the unevenness of the substrate and the closing of pores because the deposition will block the transport of the gas to a certain extent. The coatings deposit on the surface of the grain individually, and aluminum diffuses inward while iron and chromium diffuse outward. Bateni et al. (2011) found that the direction of aluminum diffusion is inward, from the surface into the bulk. Kobayashi and Yakou (2002) demonstrated that the diffusion coefficient of iron in aluminum is $53 \times 10^{-4}\ m^2\ s^{-1}$ (520-649 °C), higher than that of aluminum in iron, which is $1.8 \times 10^{-4}\ m^2\ s^{-1}$ (730-1400 °C).

The increasing amount of the catalyst in the powder for pack cementation raises the level of activity. In the high activity mixture, the inward diffusion of coating elements is dominant, whereas for the low activity one, the outward diffusion is greater. In the case of external growth, particles from the pack will be easily trapped in the coating and the surface will become rough (Bateni, 2001; Xiang and Datta, 2004). The diffusion of aluminum from the surface to the grain interior confirmed that the coating formed predominantly through inward diffusion of aluminum from the substrate.

Chapter 4

Experimental Techniques

4.1 Freeze Tape Casting Technique

The green tapes with various concentrations of solid loading were produced by the new freeze tape casting technique. The metal tapes were cast at the Department of Mechanical and Industrial Engineering, Montana State University. Training to operate the apparatus and additional assistance to produce the tapes were provided by Stephen Sofie's group at University of Montana.

The green tapes are classified by the amount of steel powder in the mixture, as the concentration of stainless steel powder determines the green density. The 56%, 67% and 78% solid loading green tapes were fabricated in our research. For example, 56% solid loading means 56 g of steel powder out of a total weight of 100 g. The process was completed in three days:

1. First day: A Nalgene bottle containing polyacrylic acid (PAA), 0.4% carboxy methyl cellulose solvent (CMC) (water was added to produce the CMC solution one day before), YSZ balls and stainless steel powder was shaken vigorously, and then placed in the ball mill for 24 hours.
2. Second day: The polyethylene glycol (PEG) with a little hydroxyethyl cellulose (HEC) was added to the bottle while shaking and then ball milled for another 24 hours after shaking.
3. Third day: With the freeze tape caster (as shown in Figure 4.1a and b) cooled to -80℃, the mixture was poured onto the freezing bed. Figure 4.1 (c) and (d) display the doctor blade which was used to control the dimension of the aqueous slip cast onto a carrier film. Then the tape was dried in the vacuum chamber at -20℃. Different lengths and widths of the tapes were fabricated by adjusting the doctor blade.

During the preparation of casting slurry, the carboxymethyl cellulose sodium salt was used as the suspending agent, hydroxyethyl cellulose as the binder, and polyethylene glycol as the plasticizer. As described before, the tape was dried in the vacuum furnace at -20℃ after freeze tape casting, and then went through the sintering process in hydrogen. Finally a sample with a diameter of 25 mm was obtained. The surface was cleaned before coating by soaking in pure alcohol in an

ultrasonic bath. The CMC and HEC were both used as binder. The green tapes with higher solid loading had a lower content of binder. Hence the 78% green tapes were more fragile than the 56% green tapes.

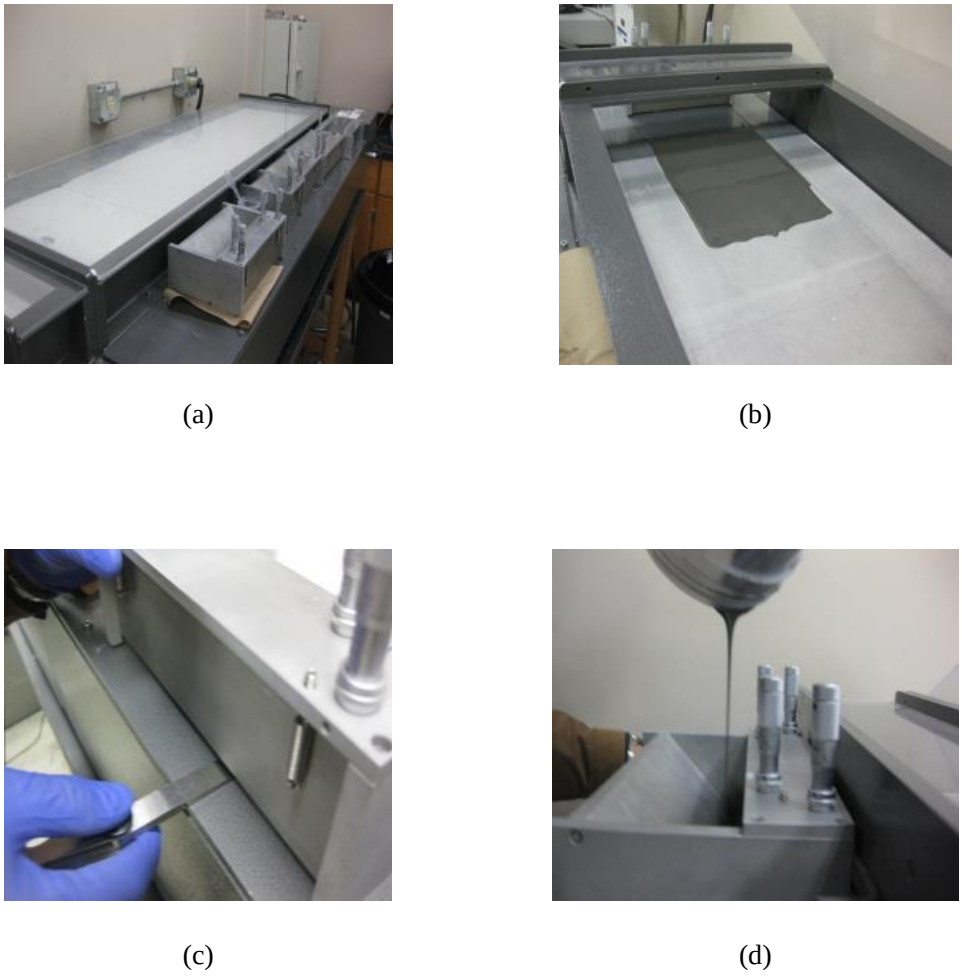

(a) (b)

(c) (d)

Figure 4.1: Freeze tape casting device of (a) freeze tape caster and doctor blade, (b) freeze tape caster, (c) adjustment of doctor blade and (d) pouring mixture into doctor blade reservoir.

4.2 Screen Printing Method

4.2.1 Screen Printing Technique

When preparing the green substrates for the screen printing process, a circle with a diameter of 28 mm was first scribed on the top of the green tape, to denote the boundary of the electrode. The thicknesses of the layers are set by the screen thickness, 80 μm in our case. An 80 μm gel application resulted in a layer of a final thickness of 40 μm because of the spreading (the materials printed twice may contribute to a total thickness of 80 μm). Later a layer of transition material was printed, followed by applying another two layers of cathode material. Then two layers of electrolyte material were applied. A smaller circle with a diameter of 20 mm needed to be marked in the center of the electrolyte layer to restrict the position of anode layer, before the final two layers of the anode material were printed on the top. The whole structure of the cell was thus completed. During the whole process, six hours of natural drying at room temperature was left between each layer. Figure 4.2 presents the structures of the screen printing device.

For anode and electrolyte, we used the ball milling to mix the powder which is called starting powder. In addition, the interdiffusion of Ni, Fe and Cr between

the supporting layer and Ni catalyst in the anode is critical for the conventional metal-supported SOFCs. Tucker et al. (2007) solved this problem by adding a barrier layer between the supporting layer and the anode layer.

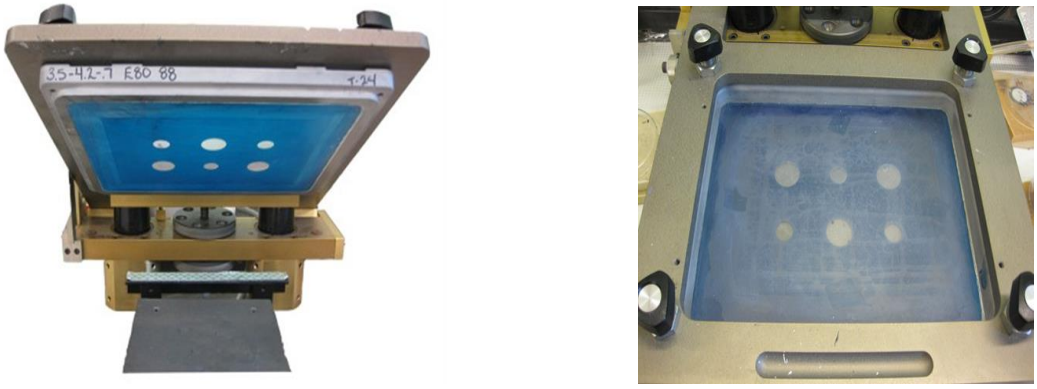

(a) (b)

Figure 4.2: Screen printing device.

4.2.2 Gel Preparation

By using the green tapes as substrates, the transition, cathode, electrolyte and anode layers should be added on top of the substrate, layer by layer, with the screen printing technique. Because of the screen printing device, all the materials which are going to be applied as printing layers should be in a gel state. The percentage of the component determines the structure and the property of the layer.

The cells we produced had a different stacking sequence from the ones reported by Tucker et al. (2007) (as shown in Figure 2.4) from the bottom to the top. Our sequence was steel substrate, transition, cathode, electrolyte and anode layer. Table 4.1 lists the densities of all the materials in the project.

Table 4.1: Densities of the Materials.

	Density (g/cm^3)
Ni	8.90
Al_2O_3	3.96
SiC	3.10
AlN	3.26
YSZ	6.0
C	2.25
NiO	6.72
Stainless Steel 430	7.75
GDC	7.65
Ni/YSZ	6.87

As YSZ and GDC were investigated in our project, different gels were prepared with different compositions.

1. Components of each layer in the YSZ SOFC. All the powder mixtures were ball milled for 24 hours. Table 4.2 shows the components of YSZ SOFC in the project, which met all the requirements for different printing layers (Figure 4.3):

(1) Transition layer:

The mass ratio of 8YSZ: steel powder (UNS 440C, 22 μm, Sandvik

Materials Technology, Sweden): carbon (Grade 4023, Asbury Graphite Mills, Inc., USA) = 10:13:5 and the volume ratio of 8YSZ: steel powder = 1:1. Therefore, the first layer had a new proportion with the volume ratio of 8YSZ: steel powder=33:67, followed by another layer with the volume ratio of 8YSZ: steel powder=67:33.

(2) Cathode layer.

(3) Electrolyte layer:

The molar ratio of 8YSZ：Mn_2O_3=23：2.

(4) Anode layer:

The volume ratio of 8YSZ: NiO = 1:1.

Table 4.2: Components of each layer in YSZ SOFC.

Transition layer	The first layer	6.38 g 8 YSZ+16.62 g steel powder (22 μm) +5 g carbon
	The second layer	14.06 g 8 YSZ+8.94 g steel powder (22 μm) +5 g carbon
Cathode layer		20 g 8YSZ + 5 g graphite
Electrolyte layer		20 g 8YSZ + 0.935 g Mn_2O_3
Anode layer		13.44 g NiO + 11.36 g 8 YSZ+6.2 g carbon

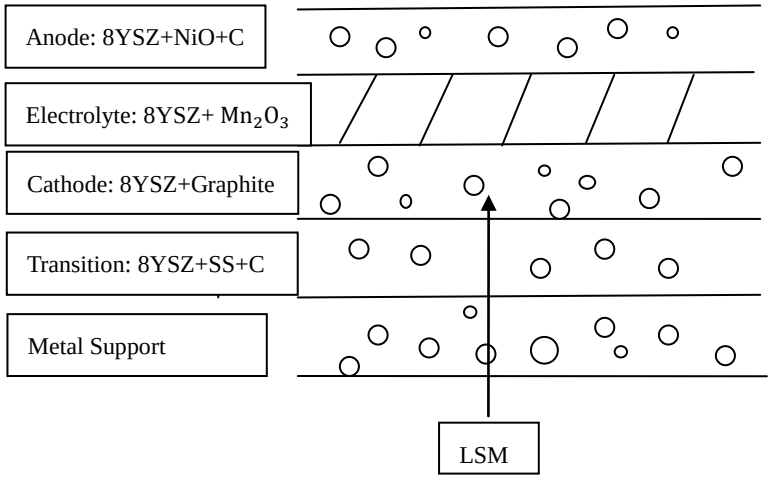

Figure 4.3: Schematic structure of YSZ SOFC.

2. Components of each layer in GDC SOFC. All the powder mixtures were ball milled for 24 hours. Table 4.3 shows the amount of material used in each layer (Figure 4.4): GDC (gadolinia doped ceria, 10% Gd_2O_3, M Grade) was tried as an alternative to YSZ. The GDC powder (GDC10-M，Fuel Cell Materials, USA) had a surface area of 35.5 m^2/g and a particle size of 0.24 μm. The nominal composition is $Gd_{0.1}Ce_{0.9}O_{2-\delta}$. In addition, the density of CeO_2 is 7.65 g/cm^3 while that of Gd_2O_3 is 7.07 g/cm^3, so the density of the GDC is taken to be 7.65 g/cm^3 as Gd is only a small amout compared with Ce. This value is almost the same with the density of UNS 440, which is 7.65 g/cm^3. Consequently, if the volume ratio of GDC and steel powder (22 μm) = 1:1 needs to be maintained, the mass ratio should also be 1:1 as their densities are

assumed to be equal. There are some conditions required for printing different layers:

(1) Transition layer.

According to the volume ratio of GDC: steel powder = 1:1, as discussed before, the densities of the two materials are assumed to be the same, which means that the mass ratio of GDC: steel powder (22 μm) = 1:1. Consequently, the mass ratio of GDC: steel powder (22 μm): carbon = 2.3: 2.3: 1.

(2) Cathode layer:

Two different kinds of cathode materials were applied. One was the combination of GDC and graphite (M450, the Asbury Graphite Mills, Inc., USA), and the other was the mixture of GDC and PMMA (polymethyl methacrylate). PMMA and graphite have the same function of forming the porous structure. However, the graphite can't be used in the ball-milling process as it doesn't maintain its shape. Two groups of cells classified by two kinds of cathode materials were produced to determine the different influences of graphite and PMMA.

(3) Electrolyte layer.

(4) Anode layer:

The anode layer had the same components of GDC and PMMA with the

cathode layer.

As an alternative to the previous anode layer consisting of 8YSZ and NiO, Ni was removed because of its larger thermal expansion. It can be added as $Ni(NO_3)_2$ by infiltration after sintering. Therefore, during the infiltration process, as for the cathode, the LSM solvent can flow through metal-support layer and transition layer, and then finally permeate the cathode layer; as for the anode, the $Ni(NO_3)_2$ solvent is infiltrated into the anode layer as illustrated in Figure 4.4. Two groups of cells classified by the different components of cathode were produced:

Group 1: The cathode matrix consisted of GDC and graphite.

Group 2: The cathode matrix consisted of GDC and PMMA.

Table 4.3: Components of each layer in GDC SOFC.

Transition layer	11.5 g GDC+11.5 g steel powder (22 μm) +5 g carbon
Cathode layer	20 g GDC + 5 g graphite (M 450) / 30 μm PMMA
Electrolyte layer	25 g GDC powder
Anode layer	20 g GDC + 5 g 30 μm PMMA

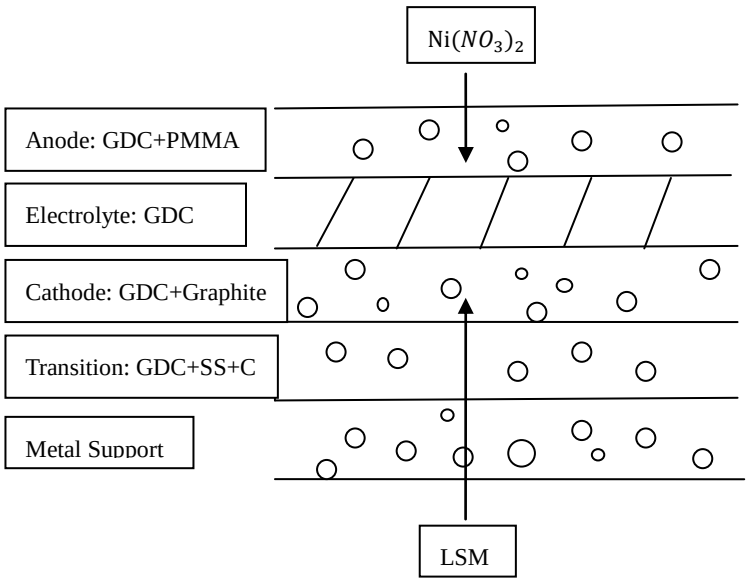

Figure 4.4: Schematic structure of GDC SOFC.

4.3 Pack Cementation Technique

As mentioned before, the materials used in the pack cementation process consisted of Al powder (-325 mesh, 99.5%, metals basis, Alfa Aesar, USA) as the metal source, Al_2O_3 (α-phase, 99.9%, metals basis, Alfa Aesar, USA) as the permeable separator and NH_4Cl (Caledon Laboratory Chemicals, Canada) as the activator.

The parameters which affect the pack cementation process are temperature, proportion of each component and duration at the reaction temperature. Different

ratios of mixtures were tested to determine the optimum proportion for the pack cementation. A horizontal furnace was used in the pack cementation coating process. An aluminia crucible and lid were selected to fit into the horizontal furnace. The container was partly filled with pack cementation powder, and then the fired metal tape was inserted and the balance filled with powder as shown in Figure 4.5. Then the container with sample was placed in the furnace tube. Argon flow was applied during the whole process including heating and cooling in order to avoid oxidation. When the furnace cooled down to room temperature, the sample was taken out and sonicated in ethanol (ultrasonication) for half an hour to loosen the powder impurities on the surface.

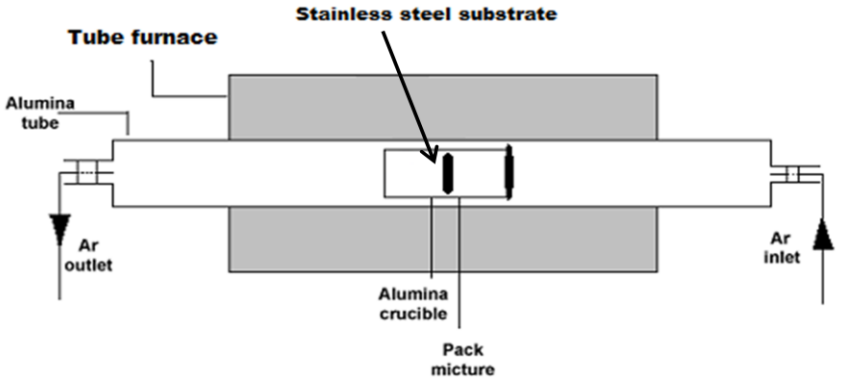

Figure 4.5: Tube furnace for pack cementation (Bateni, 2011).

Table 4.4: Percentages of the different mixtures.

	1	2	3	4
Al (wt%)	3	4	5	7
NH_4Cl (wt%)	5	5	5	5
Al_2O_3 (wt%)	92	91	90	88

Table 4.4 lists four mixtures classified by different ratios and used in the project. The percentage of the mixed powder was calculated by weight and the percentage of NH_4Cl was fixed. The amount of NH_4Cl was set constant (5 wt%), while the sum of Al_2O_3 and Al was always 95 wt%. Several different conditions were compared: 700℃ and 800℃ for half an hour, one hour and two hours. The samples were analyzed by JEOL 6610 scanning electron microscope SEM with attached energy-dispersive X-ray spectrometer (EDS).

Chapter 5

Relative Shrinkage Measurements

Due to the difficulty of co-sintering the complete cell, a series of experiments were performed to test the relative shrinkage rates of different components. When the relative shrinkages of the metal and ceramic layers are close to each other during processing of composites, it is less likely that the cracks and delamination will occur.

5.1 Relative Shrinkage Calculation

As mentioned before, the green tapes were classified by the solid loading or the amount of steel powder in the mixture which determines the degree of green density. A series of experiments were conducted on samples of various thicknesses from 1100°C to 1300°C. The thinner tapes were usually less than 1

mm and the thicker ones generally varied from 1 mm to 2.2 mm. In addition, holding time at sintering temperature was also varied. The size of the cast tape was 190 mm × 270 mm (Figure 5.1). Generally, a piece of tape could be cut into 50 button cells by a 31.5 mm diameter punch. The relative shrinkage of the green tape was measured under different conditions in order to check their compatibility with other cell components. Normally, a burn-out process was necessary before high-temperature co-sintering, which removed the organic binder in the green tape by slow heating to 600°C.

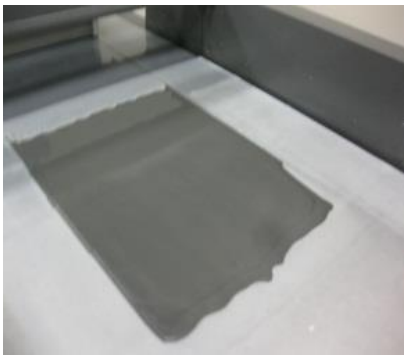

Figure 5.1: Green tape.

In the burn-out furnace, the temperature profile was set as follows: ramp up from RT to 185℃ at a rate of 5℃/min, hold at 185℃ for 3 hours, heat to 400℃ and hold for 4 hours, heat to 600℃ and hold for 3 hours, cool to RT (Figure 5.2). After the burn-out process, the sample was taken out and transferred to another

furnace for sintering.

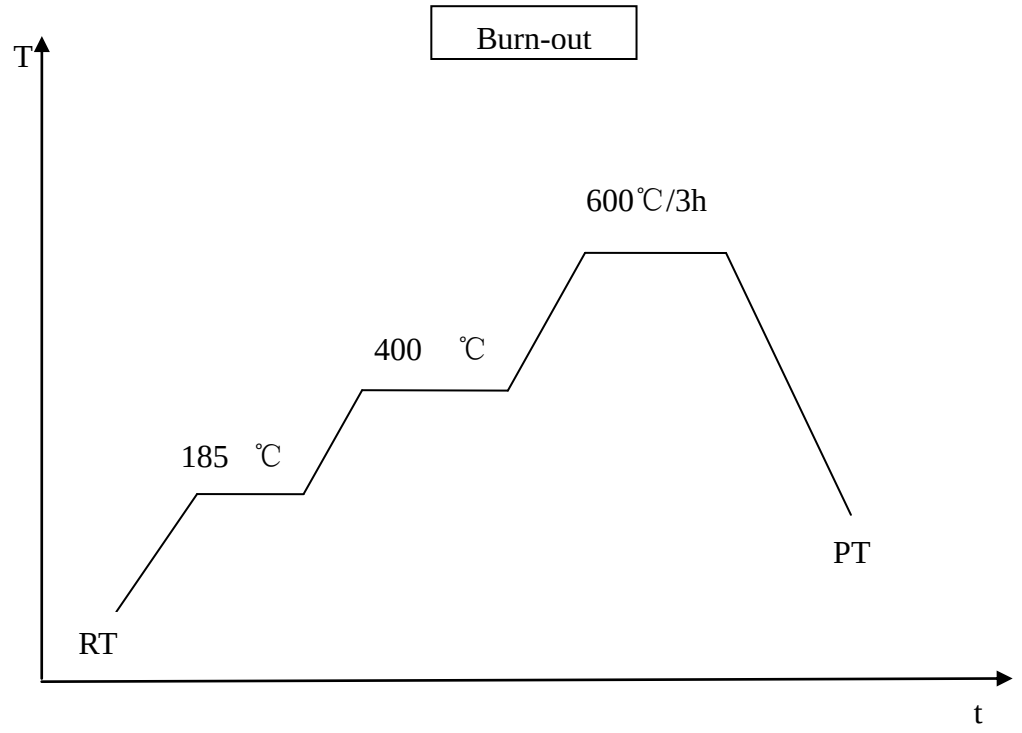

Figure 5.2: Burn-out schedule.

The relative shrinkage of the green tape was calculated by the equation below:

$$\text{Relative Shrinkage} = \left(\frac{d_o - d_f}{d_o}\right) \times 100\% \qquad (5.1)$$

in which d_o is the original diameter of the green tape before sintering and d_f is the final average diameter of the green tape after sintering, calculated by averaging all the diameters $(d_1, d_2, \ldots, d_n)$ measured in different directions:

$$d_f = \frac{d_1 + d_2 + \cdots + d_n}{n} \qquad (5.2)$$

5.2 Relative Shrinkage of Electrolyte

Measuring the relative shrinkage of the electrolyte was carried out in the same way. Figure 5.3 shows the rate and amount of shrinkage (with and without burn-out) for YSZ electrolyte. All the samples were sintered in dry H_2 at 1300℃. The sample subjected to burn-out shows more rapid shrinkage. Therefore, it is necessary to find a schedule for sintering the complete cell that matches the relative shrinkage of the electrolyte and achieves a maximum relative shrinkage value around 20% (with burning out) and 15% (without burning out) at 4 hours.

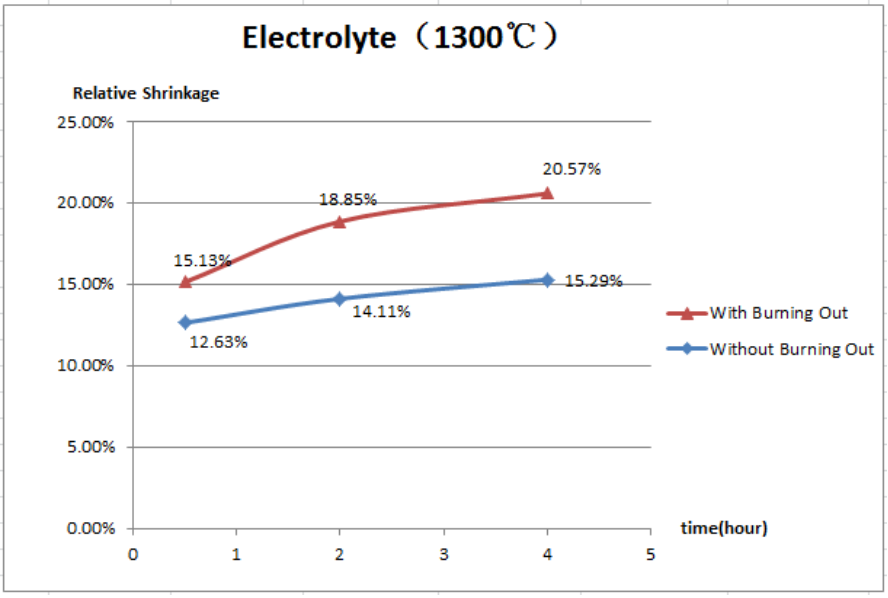

Figure 5.3: Comparison between relative shrinkages for YSZ electrolyte with and without burn-out.

5.3 Effect of Different Parameters for Green Tapes

5.3.1 Effect of Burn-out Process

Figure 5.4 shows a comparison of shrinkage for 56% solid loading green tapes. All the samples were sintered in dry H_2. The curves labeled as "1300°C thin" and "1300°C thin (burn out)" can be used to study the influence of burning out. During the first 1.5 hours, the relative shrinkage of "1300°C thin (burn out)" is much higher than that of "1300°C thin", but the two curves almost meet at the end at the 4-hour point. The relative shrinkage range of the sample with burning out varies less than that of the one without burning out. This is because the sample without burning out still has binder at the beginning of sintering, which will influence the amount of relative shrinkage. The binder is totally removed with heating time, enabling the relative shrinkage of the samples with and without burn-out to reach the same point.

Consequently, the burn-out process has influence on the relative shrinkage in the shorter time periods of 0.5 hour or 1 hour. However, when the duration time is extended to 4 hours or longer, the burn-out process has little influence on the

values of the relative shrinkages. As a result, the green tapes with and without burn-out can both be used for the purpose of testing relative shrinkage. However, burn-out is necessary during normal fabrication, in order to remove the large amount of organics in each layer of the cell.

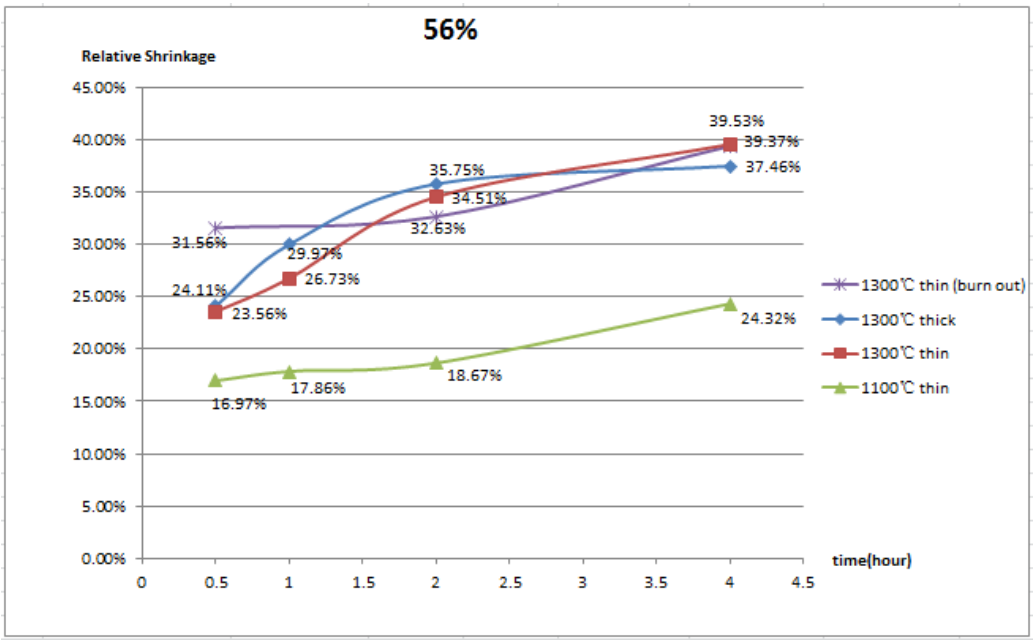

Figure 5.4: Comparison of relative shrinkage obtained for green tapes with 56% solid loading.

.

5.3.2 Effect of Wet Hydrogen

Unlike 56% and 67% green tapes, the 78% green tapes must be burned out before sintering; otherwise the tapes will break up during the sintering process. This may be caused by insufficient flexibility of the 78% green tapes. Figure 5.5 compares

the relative shrinkage of thick and thin 78% solid loading green tapes. All the samples were sintered in dry H_2 after burn-out. By comparing the shrinkage observed using dry H_2 (Figure 5.5) with that of using wet H_2 (Figure 5.6), it can be seen that the relative shrinkage of the green tape has lower values when wet H_2 is applied. Wet H_2 was produced by bubbling H_2 through a flask of distilled water. If the water is at 25°C, the wet hydrogen contains 3% H_2O. By adding water vapor to the H_2, the reducing power is lowered. This result is expected because metal sinters best in a reducing environment. The addition of humidity, i.e., oxygen, will result in oxide formation which impedes sintering.

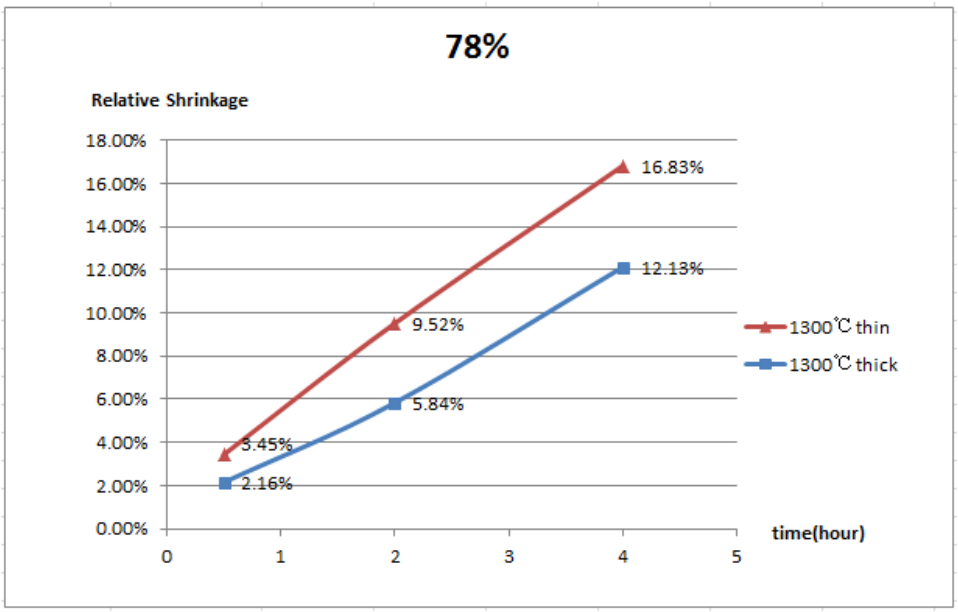

Figure 5.5: Comparison of relative shrinkage obtained for green tapes with 78% solid loading in dry H_2 (all 78% solid loading tapes are sintered with burn-out).

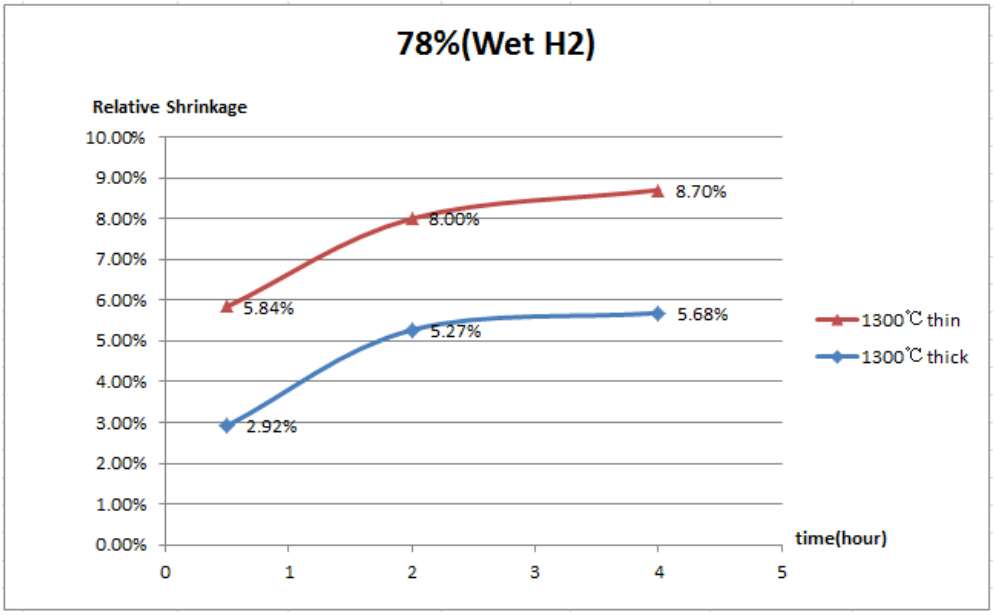

Figure 5.6: Comparison of relative shrinkage obtained for green tapes with 78% solid loading in wet H_2.

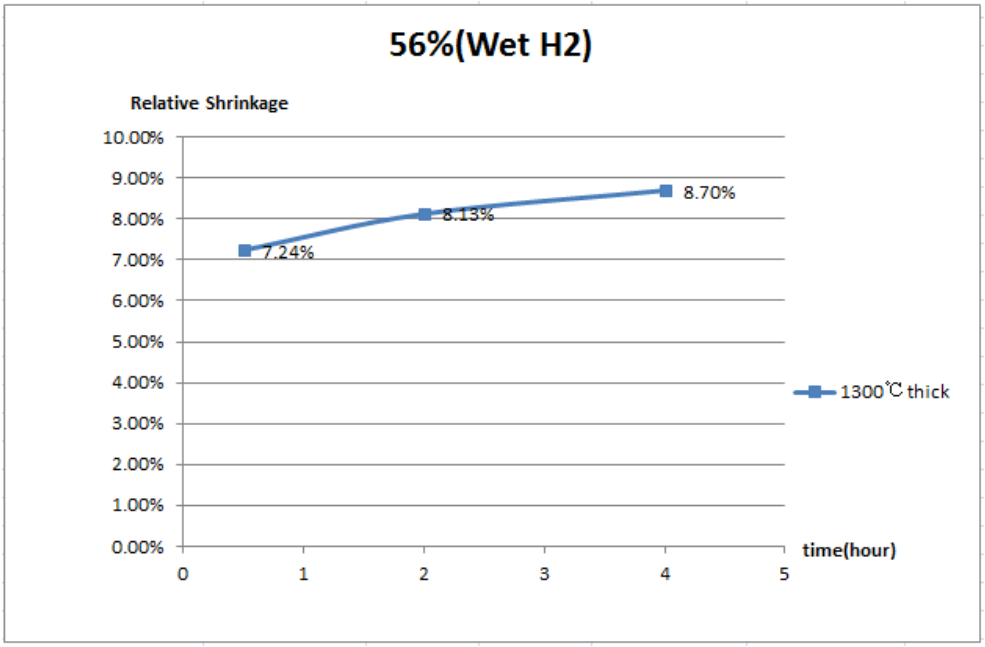

Figure 5.7: Green tape with 56% solid loading in wet H_2.

Figure 5.7 shows the 56% solid loading green tape sintered in wet H_2 after burning out. The effect of wet H_2 to retard the relative shrinkage rate is also seen by comparing the "1300°C thin (burn out)" curve in Figure 5.4 (the relative shrinkage increases from 31.6 to 39.4% within 4 hours) and the curve in Figure 5.7 (the relative shrinkage changes only from 7.2% to 8.7% within 4 hours). The former is sintered in dry H_2 while the latter in wet H_2, with all the other conditions the same.

5.3.3 Effect of Thickness and Solid Loading Percentage

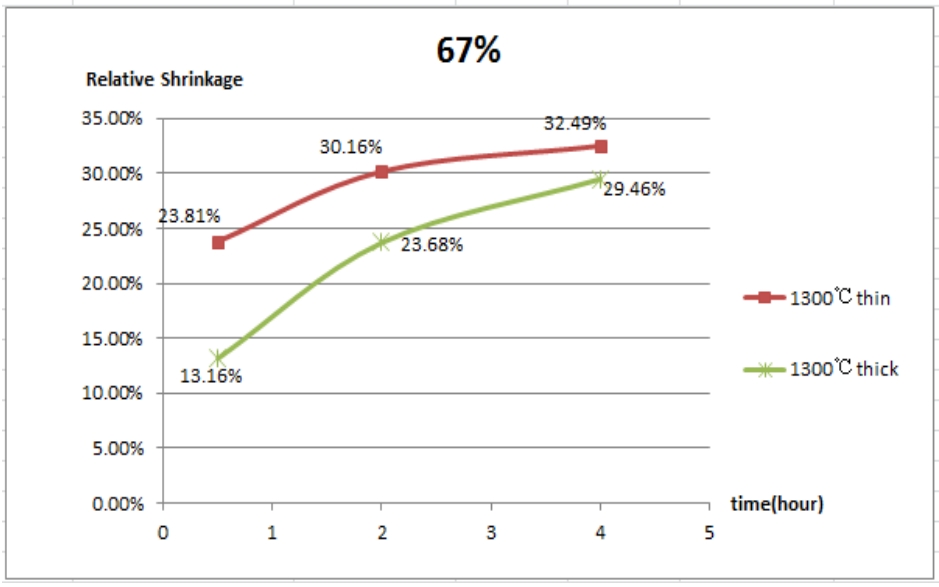

Figure 5.8: Comparison of relative shrinkage obtained for green tapes with 67% solid loading in dry H_2.

Figure 5.8 shows the difference between sintering thin and thick tapes at 67% solid loading. All the samples were sintered in dry H_2 without burn-out. It can be observed that the relative shrinkage decreases with increasing tape thickness at constant temperature. The same trend can also be observed for tapes with 56% and 78% solid loading.

For the "1300℃ thin" sample, the relative shrinkage range from 23.81 to 32.49% is lower than 23.56 to 39.53% in the green tapes with 56% solid loading (Figure 5.4). We may conclude that tapes with higher solid loading have lower relative shrinkage.

Thickness and solid-loading are both factors influencing the relative shrinkage. The relative shrinkage is inversely proportional to the thickness. Furthermore, the increase of the solid-loading percentage in green tape leads to the relatively lower shrinkage. Since the green tape with higher solid loading has less open space after burning out, it does not allow as much room for shrinking.

5.4 Conclusions

1. During the relative shrinkage measurement experiments, some conclusions are drawn for various kinds of green tapes. At lower temperatures of 1100℃, the values of relative shrinkages are smaller and thus match that of the electrolyte.

However, only the samples sintered at 1300℃ can meet the requirements due to the reason that the metal support layer needs to be reduced well. Well-reduced samples can be distinguished by the metallic color or the magnetic attraction. Similarly, when the duration time is relatively short, 1 hour in our case, the sintering is insufficient judging from the color, indicating that the sample is less sintered and partially oxidized. Normally the sintering process requires 1300℃ for 4 hours.

2. Smaller relative shrinkage can be obtained by shortening the duration time, lowering the temperature, enlarging the thickness and increasing the percentage of solid loading in the sample.
3. The 78% green tapes are much more fragile than the others after sintering and more crack-prone especially when the cathode, electrolyte and anode layers are attached during co-sintering. Therefore, the green tape with 78% solid loading is not recommended as the metal support because of less flexibility.
4. During co-sintering, a combination of wet and dry H_2 should be considered to match the green tape with electrolyte.
5. As illustrated in Figure 5.9, the curves of the green tapes with 67% and 78% solid loading are closer to that of the electrolyte. Generally speaking, the relative shrinkage of the electrolyte is smaller than that of the 67% green tape

and larger than that of the 78% one within 4 hours sintering. In addition, the thickness of the 67% green tape is 1.5 mm and that of the 78% one is 0.7 mm. As a result, a green tape with 74% solid loading and a thickness of 1.3 mm is recommended when casting the metal support for shrinkage match with the YSZ electrolyte.

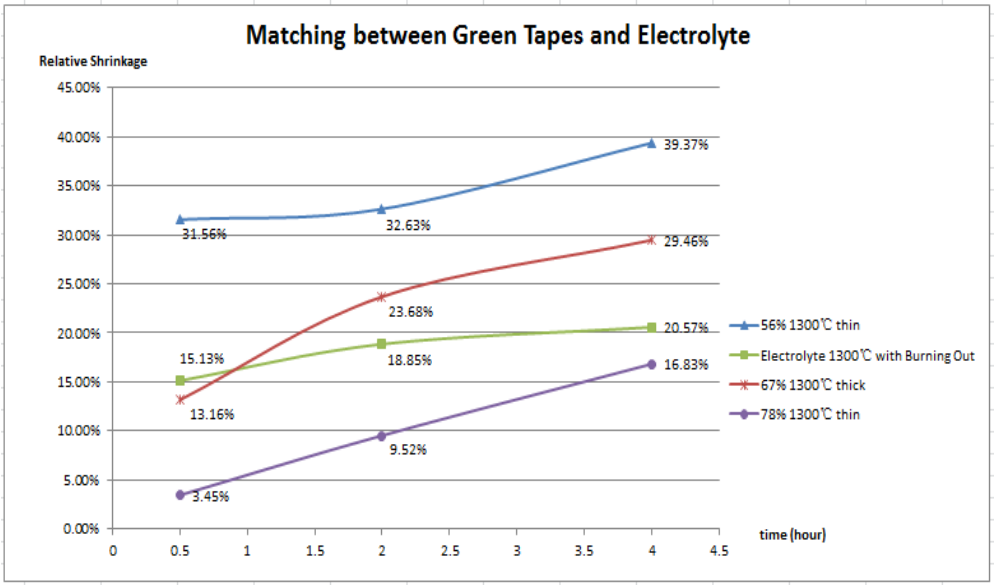

Figure 5.9: Comparison of relative shrinkage obtained for the electrolyte and green tapes with 56%, 67% and 78% solid loading.

Chapter 6

Co-sintering of the Cell

As mentioned in Section 2.5.1, the previous cells reported by Tucker et al. (2007) (shown in Figure 2.4) had cell layers in the sequence, steel substrate, anode, electrolyte and cathode from the bottom to the top. The cell we produced has the sequence, steel substrate, transition layer, cathode, electrolyte and anode from the bottom up. In the former method, cell performance suffered from poor electron conduction between the ceramic cathode and interconnect. In addition, Ni particles in the anode diffused into the metal substrate, causing transformation to α phase of stainless steel, with a larger thermal expansion and a loss of Ni in the anode. Printing the transition layer directly on the metal substrate achieved a good connection as the two layers were both metallic.

For good perforemance, cells should have the following properties after co-sintering:

1. The cell should be flat.
2. The color of the electrolyte layer should be transparent.
3. The metallic support layer should be reduced totally, as evident from metallic color or magnetic attraction.
4. No delamination or cracks.

6.1 Burn-out and Sintering Schedule

There were two burn-out programs tested in the research; the first one was illustrated in Figure 5.2 which is called “Burning Out” in the following images of the whole cell. The second way was to complete the burn-out and sintering processes in the same furnace which is termed “Program 1” to be distinguished from “Burn-out”.

The two burning out programs were similar except for one obvious difference: in the first method, the start and the finish temperature were both room temperature. For the second method, the temperature was raised from room temperature to 600℃ and then went back to 550℃ which is shown as present temperature (PT) in the diagram. The next program followed without cooling down to room temperature, in an attempt to prevent cracking. The cell with cracks

could not be used in the sintering process as the cracks are permanent once they form.

During the sintering process, the temperature was raised from PT at a rate of 6℃/min, slightly different from that of the burn-out process (5℃/min), then held at 1300℃ for different duration times (usually 0.5 hour, 1 hour or 4 hours) because of the different experimental objectives. It was then cooled down to RT (Figure 6.1).

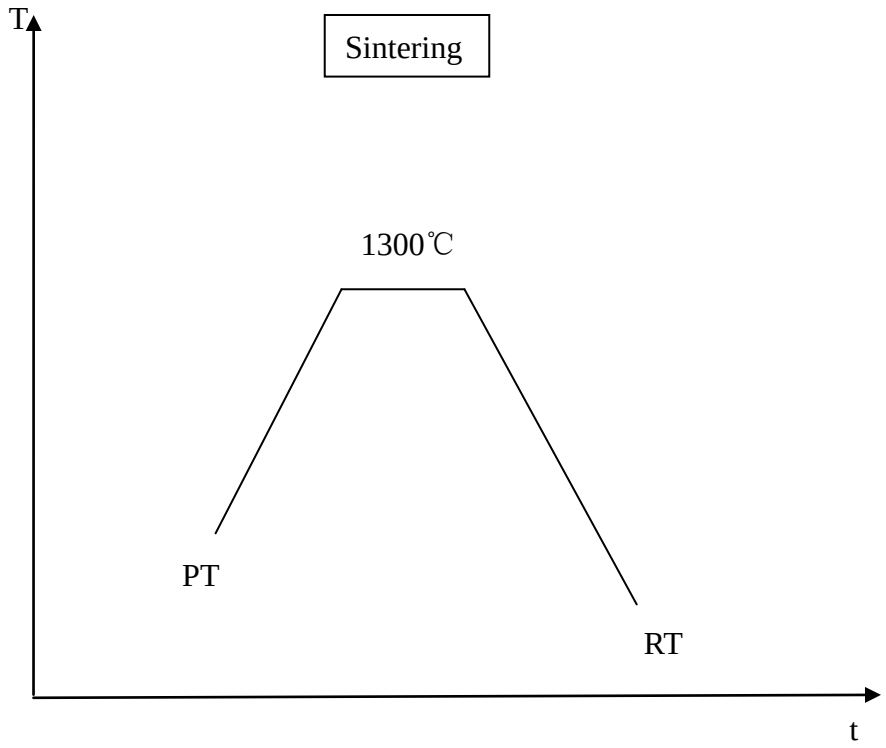

Figure 6.1: Sintering Program.

6.2 Sintering of YSZ Electrolyte

6.2.1 Effect of Wet and Dry Hydrogen

Dry hydrogen was obtained from the hydrogen cylinder directly, while the wet hydrogen passed through a water bubbler before entering the furnace, resulting in a 3% H_2O content. H_2O decomposes as shown in the equation below:

$$H_2O = H_2 + \frac{1}{2}O_2 \qquad (6.1)$$

The H_2/H_2O ratio sets the oxygen pressure of the gas by the equilibrium constant which determines the oxidizing power. At room temperature (25℃), 0.0313 atm of water vapor is obtained at equilibrium.

The pressure of oxygen gas in the atmosphere will speed up the sintering of ceramics. On the other hand, sintering of the metal powder will be retarded by formation of an oxide layer. Therefore, controlling the partial pressure of oxygen of the atmosphere can be useful in controlling the rate of sintering of metal and oxide phases.

As shown in Figure 6.2, the left cell tends to warp upward when the ceramic electrolyte shrinks faster than the metal substrate caused by excess moisture in the hydrogen. The right cell, on the contrary, shows warping downward as the metal

shrinks faster than the ceramic in dry hydrogen. Cracks appeared in both situations through different mechanisms.

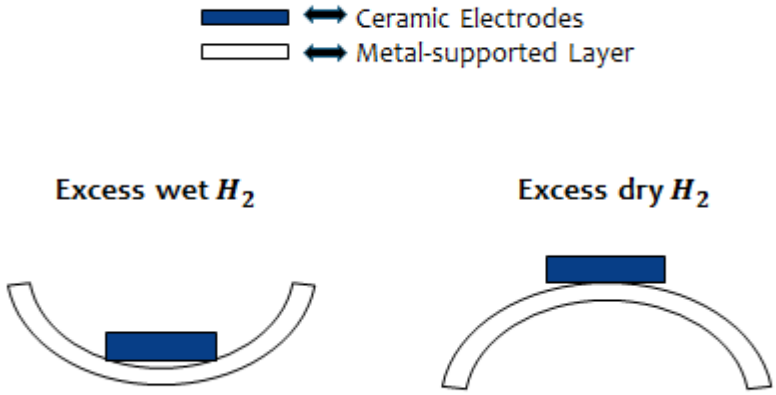

Figure 6.2: Effect of wet and dry hydrogen.

6.2.2 Effect of Wet/Dry Hydrogen Ratio

(S14) 56%: program 1+ sintering (1h), 1 h wet H_2 (1300℃)	(S10) 56%: program 1+ sintering (4h), 1.5h wet H_2 and 2.5h dry H_2 (1300℃)	(S13)56%: program 1+ sintering (4h), 20 min wet H_2 (1180℃-1300℃), 4h dry H_2 (1300℃)
(a)	(b)	(c)

Figure 6.3: (a) sample 14, (b) sample 10 and (c) sample 13.

Figure 6.3 shows the three samples made from the 56% green tape, the only difference being the exposure time to wet hydrogen at 1300℃. Sample 14 was held at 1300℃ for only 1 hour. Although the surface was flat, the sample was not sintered well as the color of the electrolyte wasn't transparent and the metal layer was not magnetic.

When the duration time at 1300℃ was extended to 4 hours, as for sample 10, sintering was improved as the electrolyte was more transparent. However, the upward warping metal-support substrate indicated the wet H_2 flow was excessive. To counteract this, the four-hour duration time was divided between wet and dry H_2 for sample 13. In addition, the wet H_2 flow started before the temperature reached 1300℃ and lasted for only 20 minutes. The balance of the duration time was dry H_2 flow, leading to a well sintered sample, although the substrate was obviously warped downward.

As a result, the longer duration time of dry H_2 at high temperature contributed to better sintering which was evident from the transparent electrolyte as well as the magnetic attraction of the metal support layer.

6.2.3 Effect of Prior/Post Exposure and Intermittent Wet Hydrogen

(S5) 67%: burning out + sintering (4h), 1.5h wet H_2 and 2.5h dry H_2 (1300℃)	(S17) 67%: burning out + sintering (4h), 2.5h dry H_2 and 1.5h wet H_2 (1300℃)	(S19) 67%: burning out + sintering (4h), 20min wet H_2 alternates with 40min dry H_2 (1300℃)

(a) (b) (c)

Figure 6.4: (a) sample 5, (b) sample 17 and (c) sample 19.

The three cells above were all produced in the same way: a combination of burning out and sintering for 4 hours. As illustrated in Figure 6.4, sample 5 was almost flat, which was a result of a reasonable distribution of time between wet and dry H_2, but there were some obvious cracks. Sample 17 was warped downward due to excess dry H_2, but the cracking problem was not as serious as for the first one. The total time of dry H_2 flow was 2.5 hours and the wet H_2 was 1.5 hours for both samples.

In the first case when the wet H_2 was flowed into the furnace prior to the

dry H_2, the oxide formed needed to be reduced before sintering in dry hydrogen could proceed, effectively shortening the dry hydrogen exposure time. However, in the second case when the wet H_2 was applied after 2.5 hours of dry H_2, the time of dry H_2 treatment was exactly 2.5 hours. The effective exposure time to dry H_2 may result in the difference in flatness of the samples.

Consequently, for equal duration time of wet H_2 and dry H_2, when the wet H_2 was passed prior to dry H_2, the sample was flatter (Figure 6.4a and b).

As for sample 19, the gas flow alternated between 20 minutes wet H_2 and 40 minutes dry H_2 one cycle per hour. The total duration time of wet H_2 was 80 minutes (20 minutes × 4) while the total duration time of dry H_2 was 160 minutes (40 minutes × 4) for a total sintering time at 1300℃ of 4 hours. Compared with the left sample (S5), the exposure time to wet H_2 here was smaller. However, the sample warped more than sample 5. The reason was that the sample was never fully reduced and behaved as if it were always in wet hydrogen. Excessive wet sintering caused upward warping.

For the two samples, the only difference was the continuous and intermittent wet H_2. As a consequence, under the same conditions, when the wet H_2 was continuous, the sample was flatter (Figure 6.4b and c).

6.2.4 Delamination

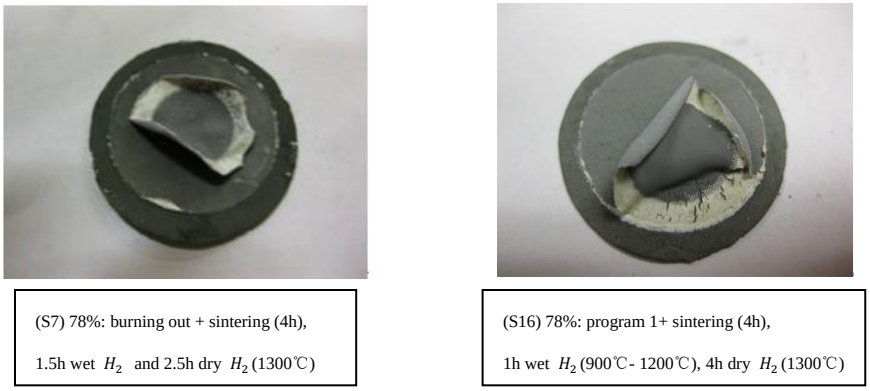

Figure 6.5: (a) sample 7 and (b) sample 16.

As shown in Figure 6.5, there was a greater chance for the appearance of delamination after co-sintering of the green tapes with 78% solid loading. The 78% green tapes were more fragile than the ones with 56% and 67%.

In other experiment, the humidity in wet hydrogen was lowered by using an ice water bath. As discussed in equation (6.1), the amount of water vapor absorbed by the hydrogen is determined by the temperature. At 0℃, 0.006 atm of water vapor at equilibrium can be obtained. Less water in the gas means less oxidation of the stainless steel. The delamination phenomenon can also be observed when the low humidity wet hydrogen was applied for the green tapes with 56% and 67% solid loading. Since maintaining the ice bath is more complicated, this method was not used (Figure 6.6).

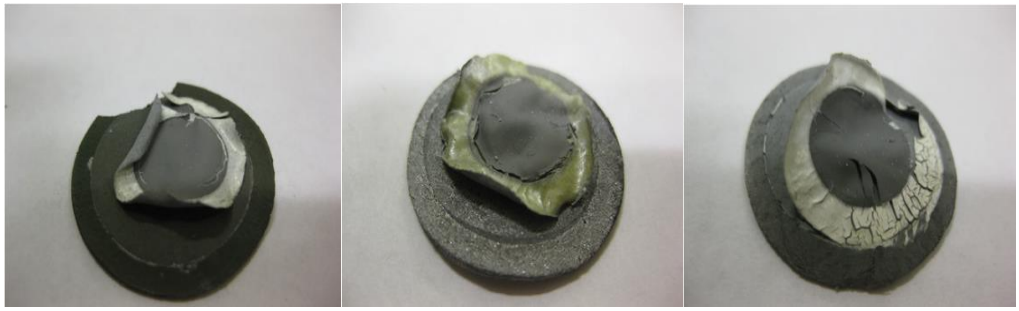

(S22) 56%: burning out + sintering (4h), 1.5h iced-wet H_2 and 2.5h dry H_2 (1300℃)	(S23) 67%: burning out + sintering (4h), 1.5h iced-wet H_2 and 2.5h dry H_2 (1300℃)	(S24) 67%: burning out + sintering (1h), 0.5h wet H_2 (900℃- 1100℃), 1h dry H_2 (1300℃)

(a) (b) (c)

Figure 6.6: (a) sample 22, (b) sample 23 and (c) sample 24.

6.2.5 Conclusions

In summary, a flat cell surface depended on a suitable distribution of wet and dry H_2. Generally, the application of prior continuous wet H_2 led to a flatter surface. A longer duration time contributed to better sintering under the premise of a reasonable balance of wet and dry H_2. Furthermore, cells with 78% solid loading metal support are not recommended for fabrication of YSZ SOFCs.

Sample 15 and sample 3 were best in terms of the flatness and the degree of sintering (Figure 6.7). However, the cracking problem was still present and could not be solved. Future experiments should focus on solving the cracking issue.

Although there were a lot of problems during the co-sintering of YSZ SOFCs, zirconia is still regarded as the most suitable electrolyte material because it is

chemically inert. Zirconia has pure ionic conduction, unlike ceria which suffers from electronic leakage. However, ceria is more conductive and easier to sinter.

(S15) 67%: program 1+ sintering (1h), 0.5h wet H_2 (900℃- 1100℃), 1h dry H_2 (1300℃)

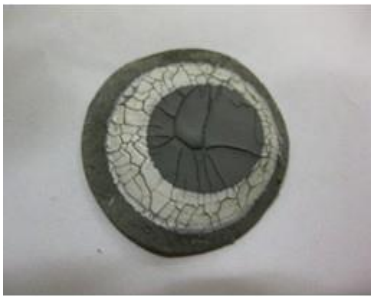

(S3) 67%: program 1+ sintering (4h), 1.5h wet H_2 and 2.5h dry H_2 (1300℃)

(a) (b)

Figure 6.7: (a) sample 15 and (b) sample 3.

6.3 Sintering of GDC Electrolyte

In the investigation of YSZ SOFCs, we observed that the cell warping was aggravated by high temperature, but lowering the temperature resulted in incomplete sintering of the electrolyte. As mentioned in Section 2.3.2, the use of GDC is amenable to lower temperature operation due to higher conductivity compared to YSZ. A series of experiments of GDC SOFCs were carried out to study the case of cell fabrication when GDC was utilized as the electrolyte.

6.3.1 GDC Powder Sintering

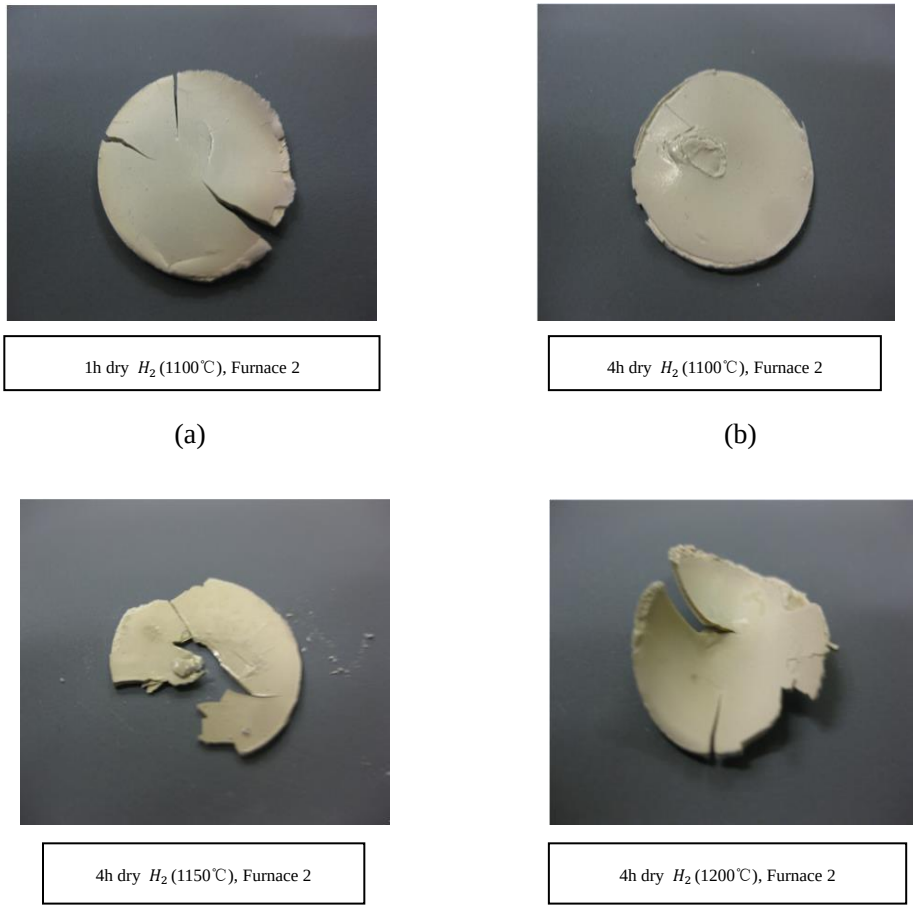

Figure 6.8: Pressed GDC tape after sintering in dry H_2 for (a) 1 hour at 1100℃, (b) 4 hours at 1100℃, (c) 4 hours at 1150℃ and (d) 4 hours at 1200℃.

Pellet samples were made from GDC powder by uniaxial pressing. The samples were sintered in dry H_2 at different temperatures including 1100℃ for 1 hour, 1100℃ for 4 hours, 1150℃ for 4 hours and 1200℃ for 4 hours (Figure

6.8). The sample sintered at 1100℃ for 4 hours (Figure 6.8b) had fewer cracks and the surface was flatter than the other three samples. Then the microstructures of the four samples were examined to identify the optimum process.

As shown in Figure 6.9, the microscopic images were taken at a magnification of 200. Among all the images, Figure 6.9 (b) shows high density with little porosity which was sintered 4 hours at 1100℃. It is the most suitable process to be used for the electrolyte material. The macroscopic structure of the sample in Figure 6.9 (b) was shown in Figure 6.8 (b) to have the fewest cracks and flattest surface. Hence the sintering schedule adopted for co-sintering experiments of GDC SOFCs was at 1100℃ for 4 hours in dry H_2.

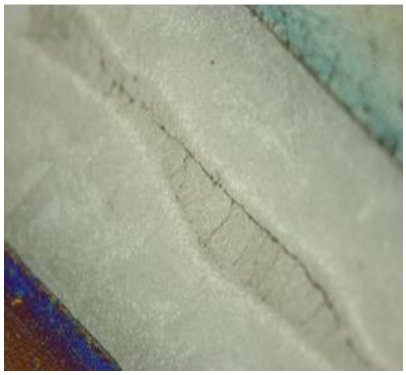

1h dry H_2 (1100℃), X 200

(a)

4h dry H_2 (1100℃), X 200

(b)

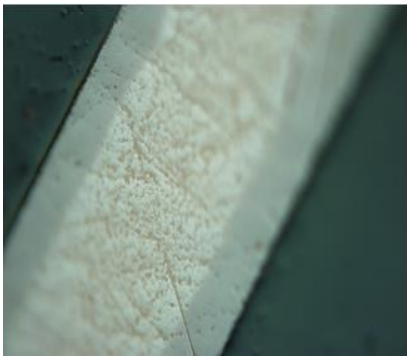

4h dry H_2 (1150℃), X 200

(c)

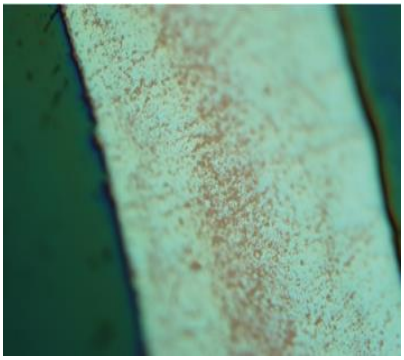

4h dry H_2 (1200℃), X 200

(d)

Figure 6.9: Microscopic images of GDC powder after sintering at a magnification of 200× for (a) (b) (c) and (d).

6.3.2 Effect of Different Furnaces

(S25) Group 1:67%: burning out + sintering (4h), 4h dry H_2 (1150℃)

(a)

(S27) Group 1:67%: burning out + sintering (4h), 4h dry H_2 (1150℃)

(b)

Figure 6.10: (a) sample 25 and (b) sample 27.

Two furnaces were utilized during the sintering process. The CM Furnace (Furnace 1) had a heating rate of 6°C/min, while the Pyrox Furnace (Furnace 2)

had a heating rate of 5°C/min. As shown in Figure 6.10, the two samples above were produced with the same fabrication conditions. The only variable was that different furnaces were used. Sample 25 sintered in Furnace 1 and sample 27 in Furnace 2 had similar results: similar relative shrinkages, similar unstable anode layers which easily delaminated, similar colors of electrolyte layer, similar color of the metal-support (evidence of the similar reduction level) as well as the same warping direction. Consequently, the different furnaces had little influence on the co-sintering results of GDC SOFC.

6.3.3 Effect of Graphite and PMMA on the Cathode

(S35) Group 2:56%: burning out + sintering (6h), 6h dry H_2 (1100℃)

(a)

(S33) Group 1:56%: burning out + sintering (6h), 6h dry H_2 (1100℃)

(b)

Figure 6.11: (a) sample 35 and (b) sample 33.

Sample 35, sintered in Furnace 2 and sample 33, sintered in Furnace 1, had

similar fabrication conditions except for the different composition of the cathode layer. The cathode layer of the left sample consisted of GDC and PMMA, while that of the right one was GDC and graphite. As the left one has more cracks and is more fragile than the right one, a conclusion can be drawn that the graphite is preferred in the cathode (Figure 6.11).

6.3.4 Ratio of Wet and Dry Hydrogen

Some conclusions from the co-sintering of YSZ SOFC also apply to the fabrication of GDC SOFC. The prior continuous wet H_2 and an appropriate distribution of wet and dry H_2 were beneficial for obtaining a flat profile of the cell. The three samples were all sintered in Furnace 1 with a different ratio of wet and dry H_2 as shown in Figure 6.12.

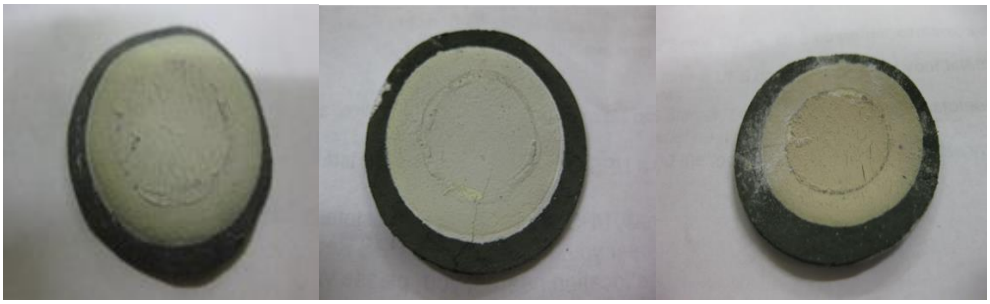

(S30) Group 1:56%: burning out + sintering (4h), 1.5h wet H_2 and 2.5h dry H_2 (1150℃)	(S34) Group 1:56%: burning out + sintering (4h), 2h wet H_2 and 2h dry H_2 (1100℃)	(S36) Group 1:56%: burning out + sintering (6h), 3h wet H_2 and 3h dry H_2 (1100℃)

(a) (b) (c)

Figure 6.12: (a) sample 30 (b) sample 34 and (c) sample 36.

(S76) Group 1:56%: burning out + sintering (6h), 3h wet H_2 and 3h dry H_2 (1100℃)

Figure 6.13: Qualified sample 76.

Sample 30 shows good integrity judging by the electrolyte and metal sintering. However, the presence of cracks and the warped downward substrate indicate excess dry H_2. Therefore, the duration time of wet and dry H_2 was adjusted to a combination of 2 hours wet hydrogen and 2 hours dry hydrogen as shown in sample 34 or for 3 hours wet hydrogen and 3 hours dry hydrogen in sample 36. The middle and the right sample both have good qualities with flat surfaces, well-sintered electrolyte and metal layers and negligible cracks. By this way, a qualified cell was fabricated with flat surface and metallic metal support, and most importantly, without any delamination or cracks as shown in Figure 6.13. Finally, compared with sample 15 and sample 3 (Figure 6.7a and b), a conclusion can be drawn that GDC SOFC can be fabricated with fewer cracks at the proper

sintering level and it’s possible to be used in the following cell testing procedure.

Chapter 7

Structural Characterization

7.1 Characterization of YSZ and GDC SOFCs

The microstructure of the sample was studied by scanning electron microscope (SEM, JEOL 6610LV) to observe the cross section of the sample and perform energy-dispersive X-ray spectrometer (EDS) analysis.

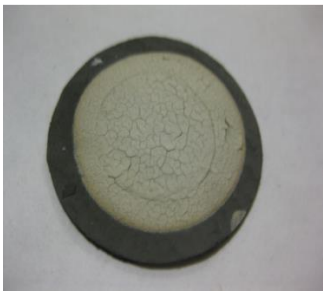

(S29) 67%: burning out + sintering (4h), 4h dry H_2 (1100℃)

(S43) Group 2:56%: burning out + sintering (4h),

(a) (b)

Figure 7.1: (a) sample 29 and (b) sample 43.

7.1.1 Characterization of the Transition Layer

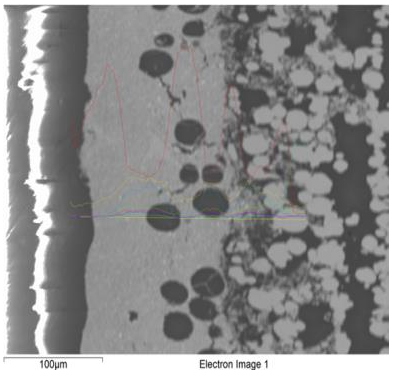

(a)

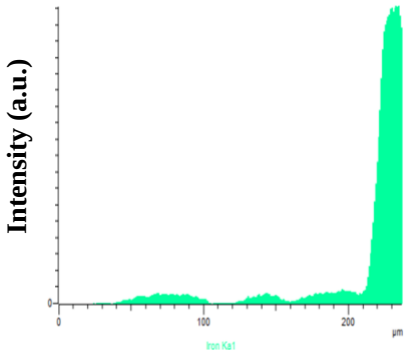

Fe

(b)

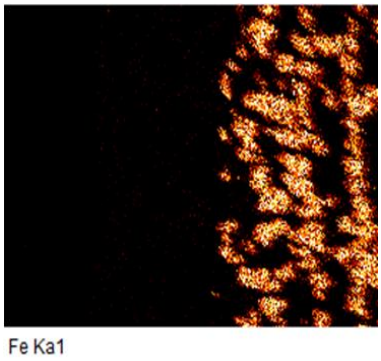

(c)

Figure 7.2: SEM micrographs and EDS analysis of Fe content in YSZ SOFC (S29): (a) and (b) line scan (the Fe peaks shows the variation of the intensity with the distance to the left boundary), (c) mapping.

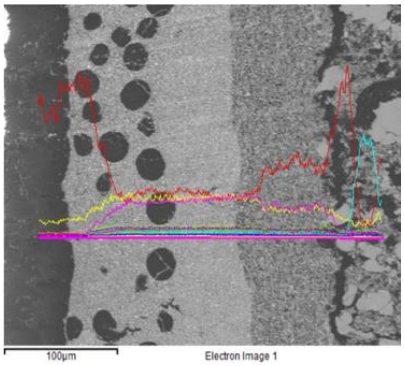

(a)

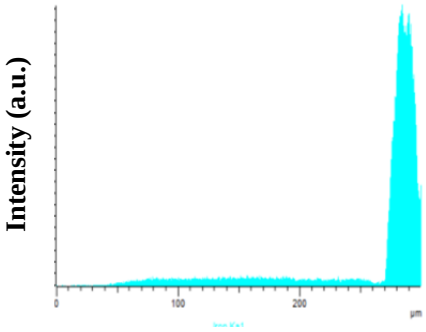

(b)

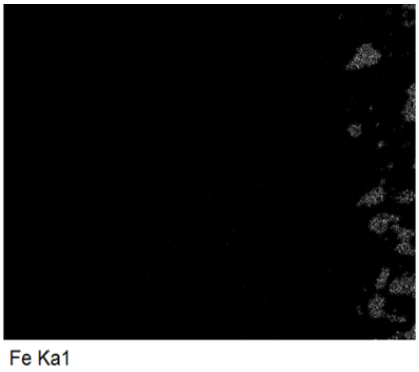

(c)

Figure 7.3: SEM micrographs and EDS analysis of Fe content in GDC SOFC (S43): (a) and (b) line scan (the Fe peaks shows the variation of the intensity with the distance to the left boundary), (c) mapping.

YSZ SOFC sample 29 and GDC SOFC sample 43 (Figure 7.1) were both sintered in Furnace 1. The results of the two types of SOFCs with metal substrates show multiple phases on the right side of Figure 7.2a and Figure 7.3a. As shown in Table 4.3 and 4.4, iron is present in the metal substrate and transition layer, but

only in a barely detectable amounts in the cathode, electrolyte and anode layers for both YSZ and GDC SOFCs. According to the EDS spectrum (Figure 7.2b and Figure 7.3b), the curves show that there is almost no Fe outside the transition layer and metal support part, as confirmed by EDS mapping.

The transition layer is used to bridge the cathode and substrate to prevent delamination. As the metal substrate has a rough surface, it's difficult to see the boundary between the transition and the metal support layers.

7.1.2 Characterization of Porous and Dense Structures

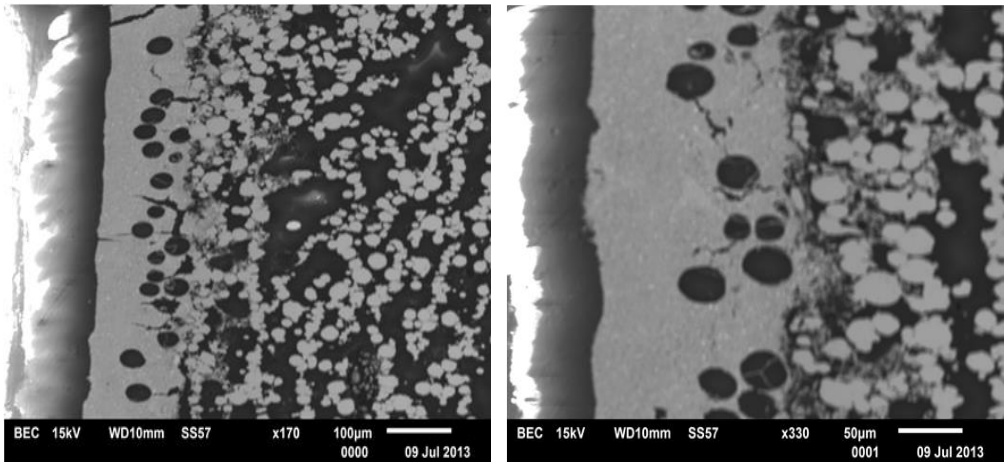

(a) (b)

Figure 7.4: SEM micrographs of YSZ SOFC (S29) at a magnification of (a) 170 and (b) 330.

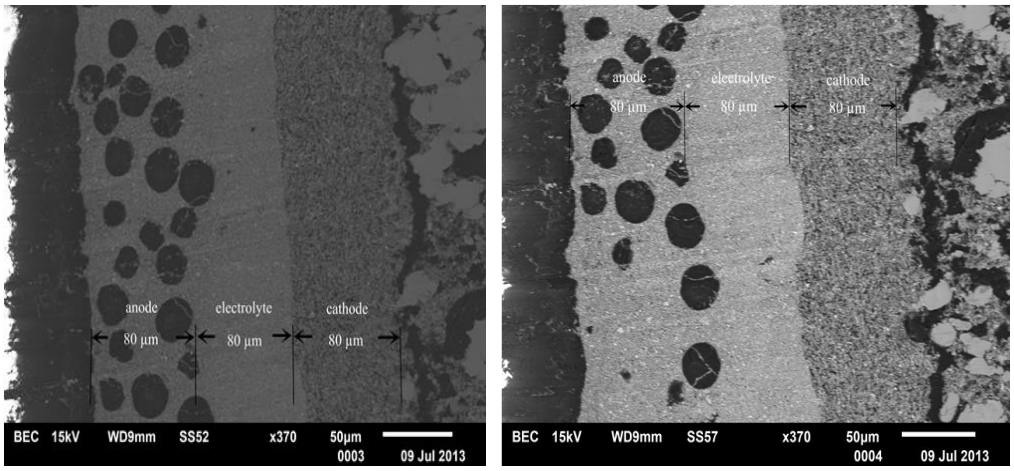

(a) (b)

Figure 7.5: SEM micrographs of GDC SOFC (S43) at a magnification of (a) 370 and (b) 370.

The two layers on the far right are the transition layer and the metal substrate with a high content of Fe. In addition, as mentioned in Section 4.2.1, each layer was screen printed to be about 80 μm thick which is consistent with the measurements from the image. The middle layer between porous anode and cathode is the electrolyte layer, which has a dense morphology. In this case, the GDC material was applied as the electrolyte. Based on the scale bar in the image, the pores are from 20-40 μm for both YSZ SOFC (Figure 7.4) and GDC SOFC (Figure 7.5). For the GDC cell, the pores can only be observed in the anode layer, and the average pore size is approximately the same as the 30 μm PMMA powder added in the anode material.

7.2 Optimization of Aluminum Coating by Pack Cementation

Since the cathode side of the fuel cell is exposed to air, the porous stainless steel support will oxidize and the oxide scale can block the pores. A good way to protect against oxidization is by an aluminum coating on all metal surfaces. This can be supplied in different ways. Sometimes the pack cementation technique is applied on the green tapes to produce the aluminum coatings as discussed in Section 3.5.

As the pack cementation was applied to coat the samples to be used in University of Toronto for their cell study, different amounts of Al, heating times and process temperatures were investigated to optimize the coating (Table 7.1). Elevated temperature and extended process time lead to a large value of weight gain after oxidation, indicating the formation of Cr_2O_3 or Fe_2O_3 scales and an insufficient aluminum protective layer. Among those samples, four groups which exhibited relatively smaller weight gain were chosen for examination.

7.2.1 Effect of Duration and Temperature

Oxidization measurements were carried out on the samples after pack cementation. An obvious conclusion from Table 7.1 is that the samples with longer duration time and higher temperature have larger weight gains.

The large weight gain after oxidation is not ideal as it indicates a large amount of oxide which might fill the pores. This might be caused by a thin layer of aluminum which is not effective as a protective layer on the porous metal support. When the Al coating is sufficiently thick to form continuous coverage and diffuse into the metal, little Cr_2O_3 would be produced, as indicated by a smaller value of weight gain. In conclusion, a thick aluminum coating that does not block the pore channels is preferred for pack cementation.

Table 7.1: Four groups of green tapes under different conditions of pack cementation.

Number	Al (wt%)	Temperature (℃)	Time (hour)	Weight Gain (%)
1	4	700	1	6.3
2	7	700	1	8.9
3	3	800	2	11.5
4	3	800	4	11.66

7.2.2 Aluminum Distribution

The morphologies of pack cementation mixtures with different components, temperature and time were characterized by SEM. Figure 7.6 shows the microstructure and EDS line scan results of the cross section of a coated green tape, obtained from pack cementation under different conditions. The peaks of Al always appear at the edges of the porous structure, which means that there is more Al at the outer surface compared to the bulk.

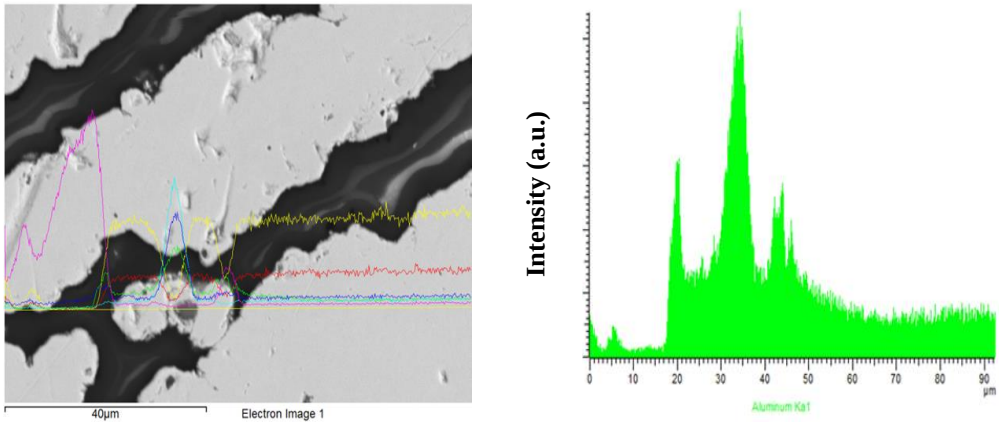

Al

(a)

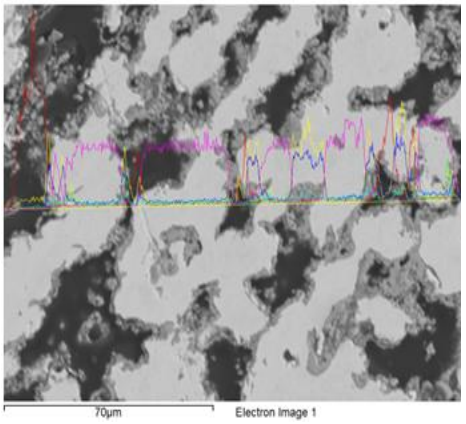
70µm
Electron Image 1

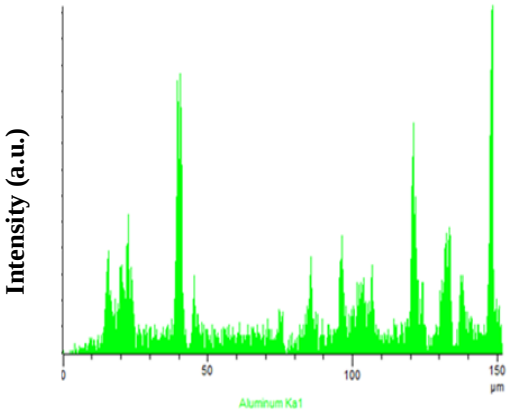
Intensity (a.u.)
0
50
100
150
µm
Aluminum Ka1

Al

(b)

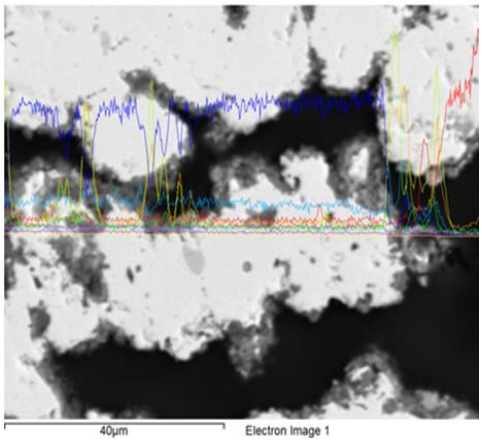
40µm
Electron Image 1

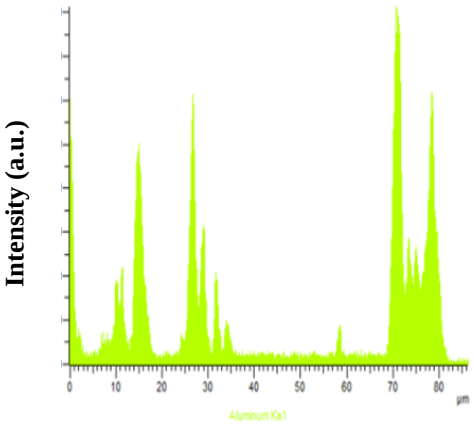
Intensity (a.u.)
0
10
20
30
40
50
60
70
80
µm
Aluminum Ka1

Al

(c)

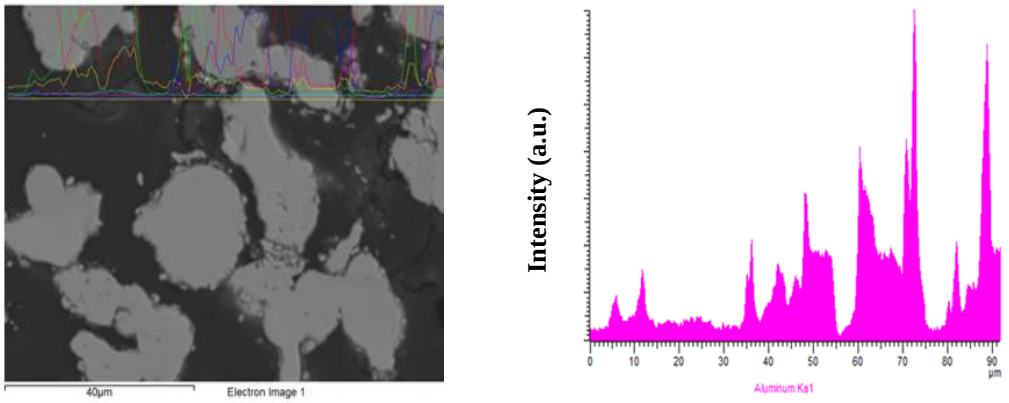

(d)

Figure 7.6: SEM micrographs and EDS line scan analysis of aluminum content in Al-coated metal substrate after pack cementation (a) at 700℃ for 1 hour with 4% Al content, (b) at 700℃ for 1 hour with 7% Al content, (c) at 800℃ for 2 hours with 3% Al content and (d) at 800℃ for 4 hours with 3% Al content. The Al peaks shows the variation of the intensity with the distance to the left boundary.

Based on the measurements in Figure 7.7, the average thickness of the aluminum coating in sample (a) is 1.28 μm. However, the Al coating is incomplete and cannot be found in some parts of the surface. The average thickness in sample (b) is about 3.75 μm, but the thick coverage sometimes blocks the pore channels. Sample (c) has the best result with an average thickness of 2.01 μm, with a uniform coverage around the grains. The aluminum coating in sample (d) is too thin to be properly observed. It had the longest duration time and the

highest temperature among the four samples, together with the lowest Al percentage in the mixture.

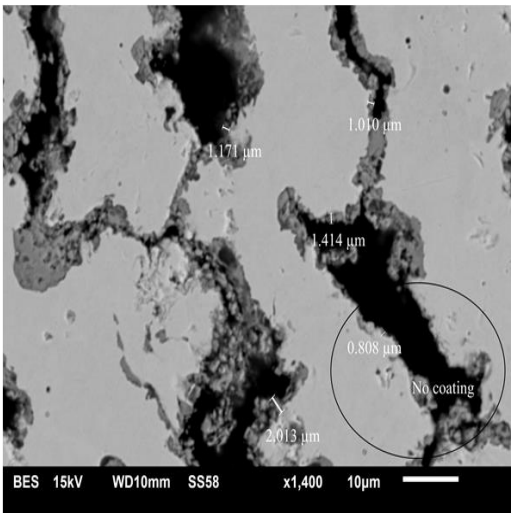

(a)

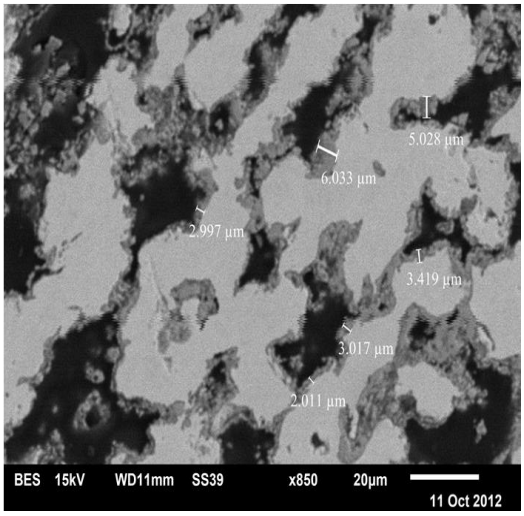

(b)

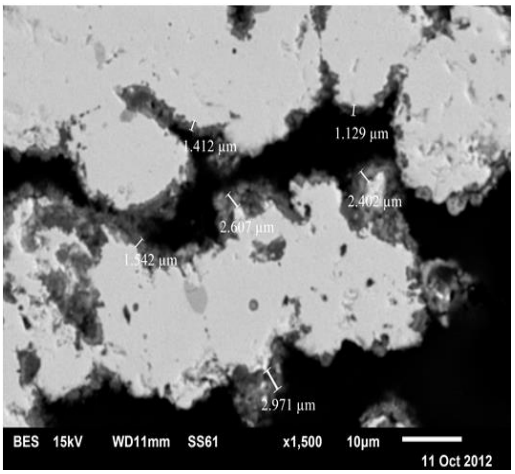

(c)

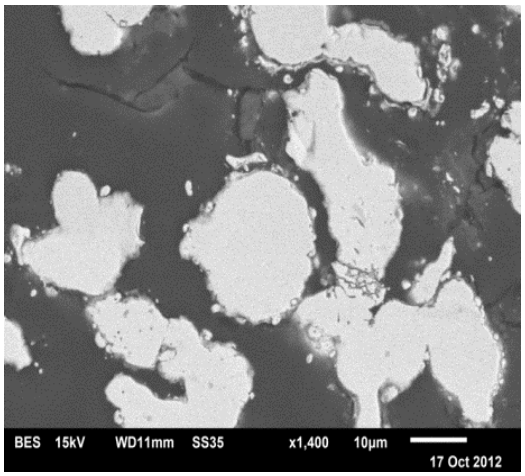

(d)

Figure 7.7: SEM micrographs of Al-coated metal substrate after pack cementation (a) at 700℃ for 1 hour with 4% Al content, (b) at 700℃ for 1 hour with 7% Al content, (c) at 800℃ for 2 hours with 3% Al content and (d) at 800℃ for 4 hours with 3% Al content.

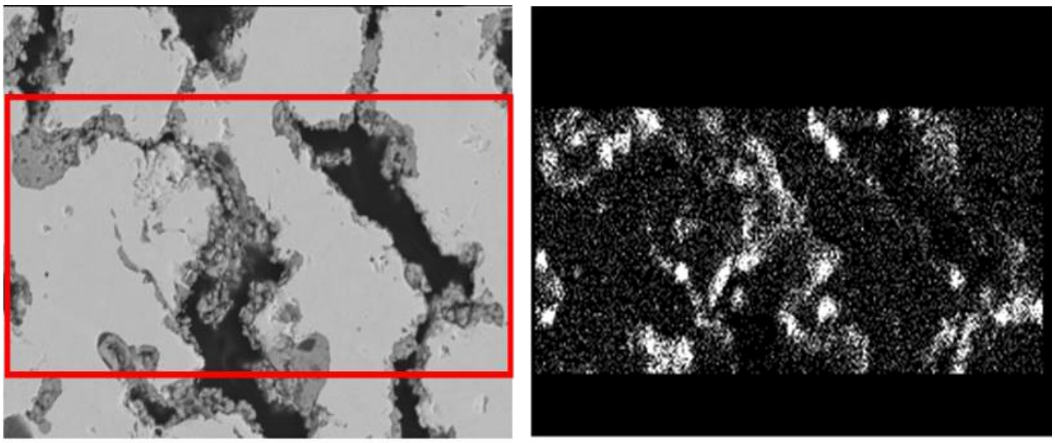

(a)

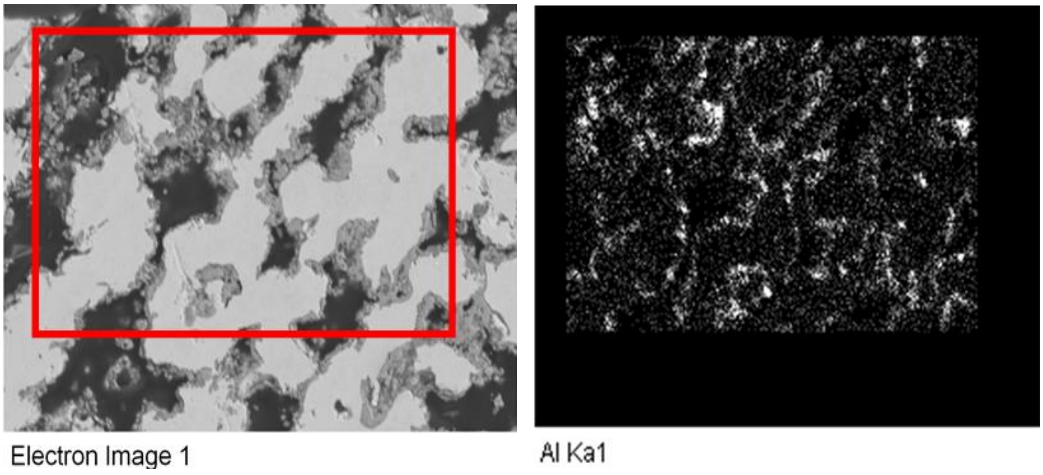

(b)

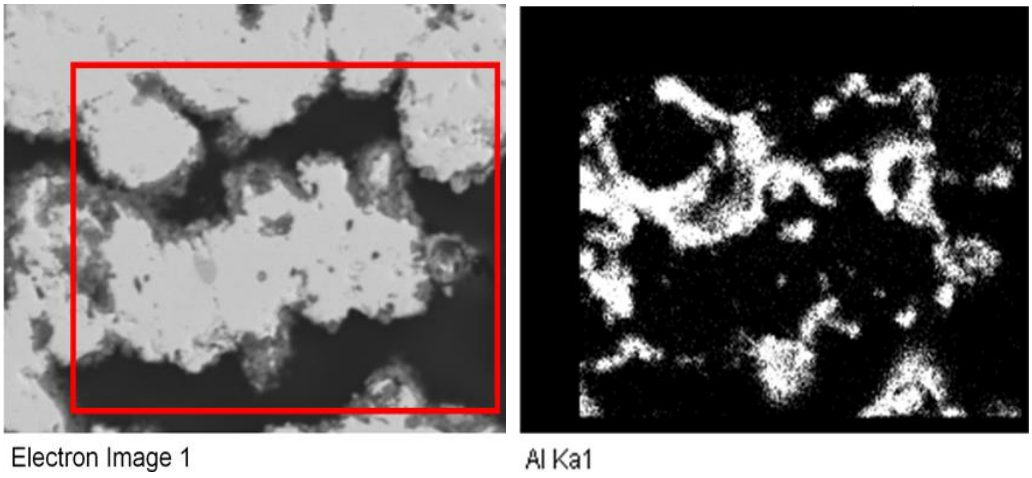

(c)

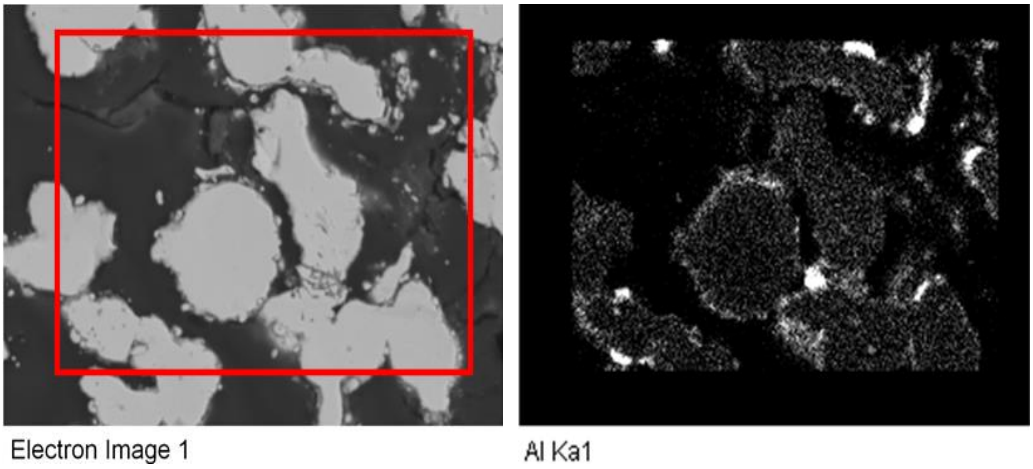

(d)

Figure 7.8: EDS mapping analysis of aluminum content in Al-coated metal substrate after pack cementation (a) at 700℃ for 1 hour with 4% Al content, (b) at 700℃ for 1 hour with 7% Al content and (c) at 800℃ for 2 hours with 3% Al content.

From the EDS mapping analysis in Figure 7.8, sample (c) shows the most consistent Al content at the grain surface, and appears to be the optimum sample

with the thickest coverage on the surface without blocking the pore channels. Consequently, pack cementation of aluminum coating at 800℃ for 2 hours with 3% Al content is recommended for the samples to University of Toronto.

Chapter 8

Summary and Conclusions

8.1 Summary

Freeze tape casting technique was utilized to fabricate the green tapes which are used as the metal support layers in SOFC, followed by the screen printing technique to print transition layer, cathode, electrolyte and anode on top of the metal substrate. Before the co-sintering, relative shrinkage measurements of the metal layers were carried out to study the influences of different parameters, including temperature, thickness and solid loading, in order to obtain a similar relative shrinkage with that of the electrolyte. During co-sintering process, YSZ and GDC SOFCs were sintered in a combination of wet and dry hydrogen atmosphere in an effort to obtain a flat surface without delamination or cracks. In addition, various Al percentage, durations and process were investigated for the pack cementation to optimize the aluminum coating,

8.2 Conclusions

Better mechanical properties can be obtained and costs reduced by using a metal support as the substrate for solid oxide fuel cells. In order to achieve good adhesion and avoid cracking upon heating, the relative shrinkage of green tapes was measured. Besides shorter duration and lower temperature, greater thickness and increasing solid loading also lead to a smaller relative shrinkage of the metal support layer which is a closer match to that of the electrolyte during sintering. Consequently, a green tape with 74% solid loading and a thickness of 1.3 mm is suggested when fabricating the green tapes in the future because of the similar relative shrinkage to that of the electrolyte.

Furthermore, it was also found that although YSZ is an effective material for the electrolyte in SOFCs, cracking and delamination problems persisted during co-sintering at high temperature. In comparison, an alternative electrolyte material, GDC showed significant advantage due to its compatibility with lower sintering temperature which resulted in fewer cracks. A suitable distribution of wet and dry H_2, and prior application of continuous wet H_2 are conducive to fabricate a flat cell.

During the pack cementation process, aluminum coating was used to form a

protective coverage on the grain surface of the green tape. The morphology of the coating can be greatly influenced by the Al content, pack cementation duration and temperature. The optimal conditions of pack cementation were found to be 3% Al in the mixture with a process temperature of 800℃ for 2 hours. The resultant coverage indicated desirable thick coverage with open pore channels.

Bibliography

Atkinson, A., Barnett, S., Gorte, R. J., et al. 2004. Advanced anodes for high-temperature fuel cells. *Nature Materials* **3**, 17 – 27

Bateni, M. R, Wei, P., Kesler, O., et al. Characterization of Aluminum coating formed on porous ferritic stainless steels by pack cementation. In preparation, 2011

Brandon, N. P., Blake, A., Corcoran, D., et al. 2004. Development of metal supported solid oxide fuel cells for operation at 500-600℃. *Journal of Fuel Cell Science and Technology*, 1(1), 61-65

Bateni, M.R., Mirdamadi, S., Ashrafizadeh, F., et al. 2001. Oxidation behaviour of titanium coated copper substrate. Surface & Coatings Technology, 139 [2-3], p.192

Christiansen, N., Hansen, J., Holm-Larsen, H., et al. 2006.Fuel Cell Seminar, HI, Honolulu

Corbin, S. F. and Apte, P. S. 1999. Engineered Porosity Via Tape Casting, Lamination and Percolation of Pyrolyzable Particulates. *Journal of the American Ceramic Society*, 82 [7] 1693.

Ebbinghaus, B. B. 1993. Thermodynamics of gas phase chromium species: the chromium oxides, the chromium oxyhydroxides and volatility calculations in waste incineration processes. Combustion and Flame, 119-137

Fergus, J. W. 2005. Metallic interconnects for solid oxide fuel cells. *Materials Science and Engineering*, A; 397(1–2):271–83

Goward, G.W. 1998. Progress in coatings for gas turbine airfoils. *Surface and Coatings Technology*, 108–109， p.73

Hilpert, K., Das, D., Miller, M., et al. 1996. Chromium vapor species over solid oxide fuel cell interconnect materials and their potential for degradation processes. *Journal of the Electrochemical Society*, 143(11),3642-3647.

Halloran, J. W. 2006. Making Better Ceramic Composites with Ice. *Science*, 311, 479–80.

Haile S. M. 2003. Fuel cell materials and components. Acta Materialia, 51(19):5981–6000.

Huang, K. and Goodenough, J.B. 2009. Solid oxide fuel cell technology: Principles, performance and operations. New Dehli: Woodhead Publishing in Energy

Jiang, S. P. and Chan, S. H. 2004. A review of anode materials development in solid oxide fuel cells. *Journal of Materials Science*, 39, 4405 – 4439

Jiang, S. P. and Wang, W. 2005. Fabrication and performance of GDC-Impregnated (La, Sr) MnO3 cathodes for intermediate temperature solid oxide fuel cells. *Journal of The Electrochemical Society*, **152** (7) A1398-A1408

Kobayashi, S. and Yakou, T. 2002. *Materials Science and Engineering*, A338, p.44

Koo, C. H., Bai, C.Y. and Luo, Y. J. 2004. The structure and high temperature corrosion behavior of pack aluminized coatings on superalloy IN-738LC. *Materials Chemistry and Physics*, 86, 258–268

Krebs, F. C. 2009. Fabrication and processing of polymer solar cells: A review of printing and coating techniques. *Solar Energy Materials & Solar Cells*, 93, 394–412

O'Hayre, R., Barnett, D.M. and Prinz, F.B. 2005. The Triple Phase Boundary- A

Mathematical Model and Experimental Investigations for Fuel Cells. *Journal of The Electrochemical Society*, 152 (2) A439-A444

Van de Graaf, M. A. C. G. and Burggraaf, A. J. 1984. in Science and Technology of Zirconia Ⅱ, N. Claussen, M. Ruhle, and A.H. Heuer (eds.). *American Ceramic Society*, Columbus, OH

Morgantown Energy Technology Center, Fuel Cells – Technology Status Report, Report No. DOE/METC-87/0257, Morgantown Energy Technology, Center, Morgantown, WV, 1986

Michaud, X. D. 2013. Electrodeposition of Co-Mn and Cu-Mn based Spinels onto lid Oxide Fuel Cell Interconnects. Open Access Dissertations and Theses. Paper 7673.

Morgensen, M. and Skaarup, S. 1996. Kinetic and geometric aspects of solid oxide fuel cell electrodes. Solid State Ionics, 86–88, part 2, page1151.

Minh, N. Q. 1993. in Science and Technology of Zirconia V, S.P.S. Badwal, M.J. Bannister, and R. H. J. Hannink (eds.), Technomic Publishing Company, Lancaster, PA, p. 652.

Minh N.Q. 1993. Ceramic fuel-cells. Journal of the American Ceramic Society, 76(3):563–88

Minh, N.Q. and Takahashi, T. 1995. *Science and Technology of ceramic fuel cells*. Elsevier.

Moritz, T. and Richter, H. J. 2006. Ceramic Bodies With Complex Geometries and Ceramic Shells by Freeze Casting Using Ice as Mold Material. *Journal of the American Ceramic Society,* 89 [8] 2394–8.

Oishi, N., Rudkin, R., Steele, B. C. H., Atkinson, A., and Brandon, N. P., 2002. Stainless Steel Supported Thick Film IT-SOFCS For Operation at 500–600 ℃. *Int. Conf. Electrophoretic Deposition: Fundamentals and Applications,* Aug 18–22, Banff, Alberta, Canada.

Petric, A. and Ling, H. 2007. Electrical conductivity and thermal expansion of spinels at elevated temnperatures. *Journal of the American Ceramic Society*, 90(5),

1515-1520.

Stephen W. Sofie, 2007, Fabrication of Functionally Graded and Aligned Porosity in Thin Ceramic Substrates With the Novel Freeze–Tape-Casting Process. *Journal of the American Ceramic Society*, 90 [7] 2024–2031

Scott, H.G. 1975. Phase relationships in the zirconia-yttria system. *Journal of materials science*, 10, 1527-1535

Sivakumar, R., Rao, E.J. 1982. An investigation of pack-aluminide coating on steel. *Oxidation of Metals*, 17, 5-6, 391

Trebbel, R., Markus, T. and Singheiser, L. 2009. Reduction of chromium evaporation with manganese-based coatings. *ECS Transactions*, 25, 1417-1422

Radovic, M. and Lara-Curzio, E. 2004. Mechanical properties of tape cast nickel-based anode materials for solid oxide fuel cells before and after reduction in hydrogen, *Acta Materialia*, 52, 5747–5756

Steele B. C. H., Heinzel, A. 2001. Materials for fuel-cell technologies. *Nature*, 414(6861):345–52.

Stubican, V.S., Hink, R.C. and Ray, S.P. 1978. Phase Equilibria and Ordering in the System ZrO_2-Y_2O_3. *Journal of the American Ceramic Society*, 61,17

Sofie, S. W. and Dogan, F. 2001. Freeze Casting of Aqueous Alumina Slurries with Glycerol. *Journal of the American Ceramic Society*, 84 [7] 1459–64.

Shao, Z. P., Zhou, W., and Zhu, Z. H. 2012. Advanced synthesis of materials for intermediate-temperature solid oxide fuel cells. *Progress in materials science*, 57, 804-874

Tucker, M. C. 2010. Progress in metal-supported solid oxide fuel cells: A review, *Journal of Power Sources*, 195, 4570–4582

Tucker, M. C., Lau, G. Y., Jacobson, C. P., et al. 2007. Performance of metal-supported SOFCs with infiltrated electrodes, *Journal of Power Sources*, 171, 477–482

T. Takahashi and Y. Suzuki, 1967, in Proceedings of Deuxiemes Journees Internationales in Proceedings of Deuxiemes Journ ées Internationales d 'Etude des Piles a Combustible, June 19-23, 1967

Sholklapper, T.Z., Lu, C., Jacobson, et al. 2006. LSM-Infiltrated Solid Oxide Fuel Cell Cathodes. *Electrochemical and Solid-State Letters*, 9(8) A376-A378

Zha, S. W., Xia, C. R. and Meng, G. Y. 2003, Effect of Gd doping on properties of ceria electrolyte for SOFCs, *Journal of Power Sources*, 115, 44–48.

Xiang, Z.D., Datta, P.K. 2004. Formation of aluminide coatings on low alloy steels at 650℃ by pack cementation process. *Materials Science and Technology*, 20 [10], p.1297